Development of a High-Frequency Isolated, Power Factor Corrected Converter.

By

Brendon Cunningham

A Thesis Submitted in Fulfilment of the Requirements for the Degree of Master of Engineering

Supervisor: Craig Baguley

Industrial Partner: IMED Ltd

School of Engineering, Computer, and Mathematical Science

AUT University

New Zealand

2020

Abstract

When marine vessels connect to shore power supplies, a galvanically isolated AC/AC power converter is typically used to convert the shore supply voltage and frequency to that required by the vessel. Commonly in industry, isolation is provided by a mains frequency transformer. Therefore, the converter size and weight are significant. Within a marine environment, this is very disadvantageous. However, through high-frequency converter operation, advances in terms of reduced size and weight can be realised.

To meet required marine vessel specifications, it is shown in this thesis that a high-frequency AC/AC converter is best implemented using a DC-link converter, as the AC input is rectified and regulated, before inversion back to AC. This thesis is concerned with the input stage of an AC/AC converter, comprising the AC/DC converter used to form the DC-link. The proposed AC/DC converter is a bridgeless isolated type, which combines high-frequency isolation, active PFC, and AC/DC conversion into a single stage using a series resonant circuit. A research gap is identified in the design of the resonant circuit necessary for this converter and thus, a design procedure is developed. This is significant, as the resonant circuit plays a crucial role in the converter operation and the ratings needed for its components. The design procedure is verified through simulation using PLECS, and the development of a prototype unit implemented with digital control and silicon carbide switching devices.

Table of Contents

List of Tables

List of Figures

Nomenclature

Acronyms

AC	Alternating Current
ADC	Analog to Digital Converter
AVG	Average
CCM	Continuous Conduction Mode
CRM	Critical Conduction Mode
CISPR	Comité International Spécial des Perturbations Radioélectriques
DC	Direct Current
DCM	Discontinuous Conduction Mode
EMC	Electromagnetic Compatibility
EMI	Electromagnetic Interference
HV	High Voltage
IC	Integrated Circuit
IEC	International Electrotechnical Commission
LV	Low Voltage
MOSFET	Metal Oxide Field Effect Transistor
PCB	Printed Circuit Board
PFC	Power Factor Correction
PID	Proportional Integral Derivative
PWM	Pulse Width Modulated
RMS	Root Mean Square
SiC	Silicon Carbide
THD	Total Harmonic Distortion
TVS	Transient Voltage Suppressor
USB	Universal Serial Bus

Key Symbols and Units

C	Capacitance (F)
D	Duty cycle $\left(\frac{t_{on}}{t_s}\right)$
f	Frequency (Hz)
f_{in}	Input frequency (Hz)
f_r	Resonant frequency (Hz)
f_s	Switching frequency (Hz)
I	Current (A)
L	Inductance (H)
n	Winding Ratio
P	Power (W)
P_{in}	Input power (W)
P_o	Output power (W)
R	Resistance (Ω)
S	Apparent Power (VA)
t_{off}	Off-time of switch (s)
t_{on}	On-time of switch (s)
t_s	Switching period (s)
V	Voltage (V)
V_{in}	Input voltage (V)
V_o	Output voltage (V)
ϕ	Phase angle between voltage and current (°)
Δ	Delta – Change in (Units) $\Delta x = \delta * x$
δ	Delta – Change in (percentage) $\Delta x = \delta * x$

Attestation of Authorship

I hereby declare that this submission is my own work and that, to the best of my knowledge and belief, it contains no material previously published or written by another person (except where explicitly defined in the acknowledgements), nor material which to a substantial extent has been submitted for the award of any other degree or diploma of a university or other institution of higher learning.

Name: Brendon Cunningham **Signature**: _____________ **Date**: 25/05/2020

Acknowledgements

Firstly, I would like to acknowledge my supervisor Craig Baguley for his patience, advice, and support during this thesis, and technical knowledge in helping me succeed in the practical areas of this research. His advice and support were instrumental and deeply appreciated.

Secondly, I would like to extend my gratitude to my industrial supervisor David Chalmers, and the entire team at IMED. Their advice and support were much appreciated, and it was great to work alongside them during this research.

Finally, I would like to thank my partner, family, and friends for their unwavering support, patience, and motivation, which helped me continue this research through to completion.

Chapter 1

Introduction

1.1 Research Background

At sea, marine vessels supply electrical loads using diesel-powered electrical generators. These generators are shut down when vessels are in port, as onboard electrical systems are run from the shore-based grid. This is desirable, as it significantly reduces pollution levels in port.

A wide range of vessels connect to shore power supplies in port. Larger vessels, such as oil tankers, cruise and cargo ships use high voltage (HV) supplies up to 15 kV [1], [2]. Medium and smaller sized recreational vessels typically use the low voltage (LV) network voltages found in the country of origin, such as 230 V, 50 Hz. As many of these vessels can travel internationally, voltage and frequency compatibility issues arise when visiting different countries, or when vessels are imported. The problems of compatibility are overcome through the use of shore power converters, which convert shore grid voltages and frequencies to those usable and rated for onboard equipment while providing galvanic isolation.

Conventionally, shore power converters are implemented using a mains frequency isolation transformer, followed by a full bridge rectifier, power factor correction (PFC) circuit, and inverter to create the AC output, as seen in Figure 1 [3].

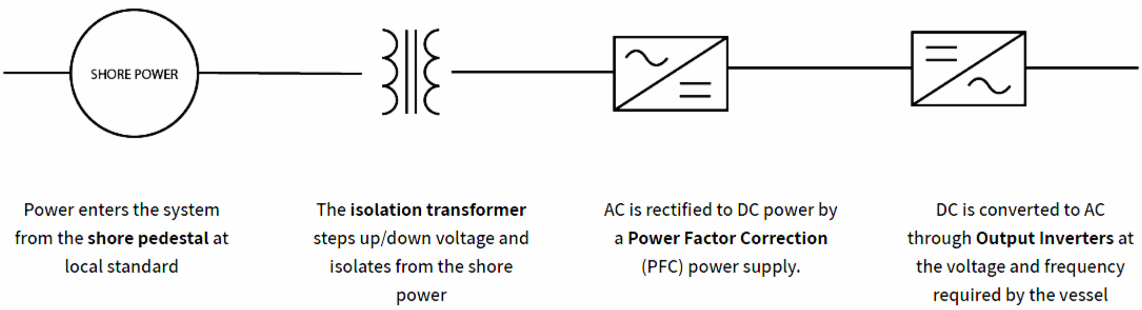

Figure 1: ASEA Power System's conversion method for shore power converters [3]

The isolation transformer is large and heavy, and the multiple stages of conversion including the full-bridge rectifier decrease efficiency, while increasing the size. Improvements are needed, particularly in terms of size and weight, as large units take up valuable onboard real estate and are difficult to maintain, due to accessibility issues. The size and weight issues of some current commercial shore power converters which use mains frequency transformers are apparent from Table 1, which compares operating power levels, weights, weight/power ratios, and efficiency levels [4]–[7].

In terms of weight and size, at least, the potential for an improved solution exists. This thesis focuses on the design of an advanced solution to overcome single-phase compatibility issues for medium-sized recreational vessels needing supply from shore-based grids of differing voltage levels and frequencies.

Table 1: Examples of commercial shore power converters

Manufacturer	Product	Power Level	Weight	Weight/Power	Efficiency	Reference
ASEA Power Systems	AC08	8 kVA	104 kg	13 kg/kVA	87%	[4]
ASEA Power Systems	AC15Q	15 kVA	154 kg	10.27 kg/kVA	89%	[5]
Atlas Marine Systems	Ultra-LP-12	12 kVA	122 kg	10.17 kg/kVA	N/A	[6]
Magnus Marine	SP100-12	12 kVA	265 kg	22.08 kg/kVA	92%	[7]
Magnus Marine	SP100-24	24 kVA	383 kg	15.96 kg/kVA	92%	[7]

1.1.1 *The Proposed Solution*

A solution to the size and weight issues associated with large, bulky, shore power converters lies in a converter that does not require a large isolation transformer and has a reduced number of stages. Potentially, this can be realised by replacing the large mains frequency isolation transformer with a high-frequency transformer of lower overall size and weight. In some existing converters, the transformer weighs up to 56% of the total weight, as described for the two-piece converters in [5], which separate the isolation transformer from the rest of the converter circuitry. An ideal solution would be to combine the isolation, active PFC, and AC/DC voltage conversion into a single-stage to replace the mains frequency isolation transformer and the PFC AC/DC converter shown Figure 1. This would allow for a lighter and more compact system that is easier to maintain.

One potential topology that meets all these requirements is the bridgeless isolated converter described in [8], shown in Figure 2. This utilizes a single-stage single-switch approach, while still being able to perform active PFC, AC/DC conversion, and provide galvanic isolation. The lack of a full bridge rectifier on the input reduces conduction losses, and fewer components reduce size and weight.

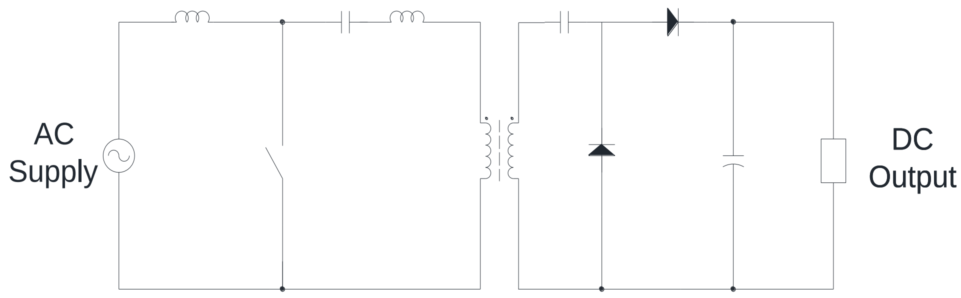

Figure 2: Bridgeless isolated converter [8]

This is a large improvement when compared to the standard two-stage and three-stage approaches of integrating a high-frequency transformer, as shown in [9], which utilize an input bridge rectifier, boost PFC stage, and DC/DC topologies to incorporate high-frequency isolation.

The bridgeless isolated converter topology shows promising potential improvements over existing methods. However, these can only be realised in a shore power converter if the topology can be scaled to the power levels required for the application, and existing concerns with the topology can be overcome. This thesis investigates and addresses these concerns. According to literature, this has not been undertaken before.

1.1.2 Requirements

This section gives an overview of essential requirements the proposed solution must satisfy, in order to be commercially viable as a shore power converter. Firstly, the transformer must provide galvanic isolation. Failure in this respect can result in harm to swimmers or any shore-side person in electrical contact with the hull or earthing in the case of an electrical fault. A transformer can also protect the vessel against any faults generated on other vessels that are not isolated, as the isolated vessel will not provide a return path to the shore earth.

By isolating the vessel's hull from the shore earth, galvanic and stray current corrosion can also be reduced. When a ship is bonded to the shore earth, the hull of the vessel can become anodic to earth, which can accelerate corrosion. Stray current corrosion can also occur when there is an earth leakage or fault current, in which the flow of the current through the hull of the vessel can cause the hull to become anodic respective to other metals in the water, including other vessels [10]. Providing isolation using a high-frequency transformer is the main area of improvement to existing shore power converter solutions, due to the size and weight savings that are potentially achievable.

Active PFC is a key requirement in the converter design. This dynamically changes the shape and phase of the input current to match that of the input voltage. This reduces harmonic content, improves power factor, and reduces line losses caused by high peak currents when the input current is non-sinusoidal. Non-sinusoidal current draw is commonly caused by the full-bridge rectifier capacitive filter found in the input stage of conventional AC/DC converters [11]. Low power factor can also be caused by other non-linear loads, or reactive loads, which draw a current that is phase-shifted with respect to the supply voltage.

As for any electrical or electronic product, a shore power converter will need to comply with various international standards such as Lloyd's Register and IEC standards on harmonic content and power factor. Limits on acceptable power factor and total harmonic distortion (THD), are outlined in many international standards, such as IEC 61000-3-12. This gives the limits of harmonic current for equipment connected to LV single-phase grid supplies that have input currents between 16 A and 75 A. Compliance with the full detail of these standards is not addressed in this research, although it is shown that the proposed solution has the ability to meet these standards.

The input voltage range of the shore power converter must be universal, from 90 to 300 V AC, and input frequencies of 50 or 60 Hz must be accommodated for. The converter must be able to supply a desired AC output voltage and frequency from any AC input voltage and frequency within specification. This requires voltage and frequency conversion over a large range. The output voltage must also be able to accommodate vessels that run various voltage and frequency configurations. Accordingly, the AC output waveform must be settable in terms of voltage (110 - 230 V AC) and frequency (50 or 60 Hz).

The prototype developed for this research must be able to supply output power of 2 kW to thoroughly evaluate its suitability as a shore power converter and explore any potential power level limitations. The design must also consider scalability, as the required power level will vary from vessel to vessel. Therefore, an evaluation of the chosen design must be undertaken to determine whether it will be suitable for future scaling when higher power levels are required. Scalability may also be achieved through modularity, where multiple smaller power level modules can be combined to achieve higher total output power, hence the initial 2 kW output power specification. Digital control is allowed for.

1.2 Research Methodology

The focus of this thesis is to investigate existing methods of AC/AC conversion to find a suitable method to be employed as a shore power converter for medium-sized recreational vessels. Once a suitable method has been identified, the limitations of the method will be analyzed and a solution will be suggested, designed, and experimentally verified.

To evaluate the suitability of specific methods of AC/AC conversion, a comprehensive literature survey is made to gather information on common methods of conversion, and each method compared against the topology requirements needed for a shore to ship power supply.

A further literature survey will be undertaken on specific topologies for the methods of conversion, to identify potential limitations. Once a suitable topology has been identified, it will be theoretically verified through simulation and experimentally verified through testing of a built prototype.

1.3 Thesis Structure

Chapter 1 explains the reasoning behind the use of an isolated AC/AC Converter in the marine industry and provides a brief insight into existing shore power converter solutions and their specifications. The key requirements for an AC/AC converter to be used as a shore power converter are also outlined, and a potential solution is suggested.

Chapter 2 is a comprehensive survey on methods of AC/AC conversion and the supporting topologies, including AC/DC input stages when utilized. This results in a second literature survey to investigate AC/DC topologies as DC-link conversion has been shown as the best way to implement the AC/AC converter. This results in an in-depth investigation of the chosen topology forming the AC/DC input stage, to identify potential limitations and gaps in existing knowledge. Research questions are then developed around a research gap regarding a design procedure required for the converter.

Chapter 3 introduces the need for a design procedure and begins the design process. The conversion ratio is derived to allow for the design of components, as this is the basis for the design procedure. This results in a fully designed converter with an optimized component design based on the design procedure.

Chapter 4 then verifies the derivation of the conversion ratio and the design procedure through multiple simulations in PLECS. Initial simulations are made without power factor correction, with further simulations integrating a power factor correction control system designed and implemented through Simulink and PLECS. This chapter then shows that the proposed topology can meet IEC standards on harmonic content.

Chapter 5 contains detail on an experimental prototype implemented using digital control, and silicon carbide switching devices. The results of the prototype confirm the theoretical design, simulation, and discuss how this relates to topology suitability as a shore to ship power supply.

Chapter 6 gives a thesis conclusion and addresses the proposed research questions. It also outlines future work that can contribute to the knowledge base of the chosen topology.

Chapter 2

Literature Review

2.1 Introduction

Isolated AC/AC power converters are required when a vessel connects to a shore power supply. These converters, referred to in the industry as shore power converters, ensure that the supplied shore power is converted to the correct voltage and frequency to suit the vessel while providing galvanic isolation. Current commercial solutions provide galvanic isolation through large and heavy low-frequency transformers. By replacing the low-frequency transformer with a high-frequency transformer, the total size and weight of the system can be reduced [12].

This chapter will cover a comprehensive literature review on methods of AC/AC conversion incorporating a high-frequency transformer but are not currently commercially used for shore power conversion. A second literature review is then conducted on the chosen method of conversion, in order to investigate the most suitable topologies to realise the method of conversion. The limitations of these topologies will be explored and used for comparison to the proposed and advanced solution investigated in the thesis.

2.2 AC/AC Literature Review Method

The IEEE Xplore database will be used to research existing topologies and perform a review to find a suitable solution that will meet the listed specifications. The initial scope of the review is to investigate the existing AC/AC converter topologies. The literature survey is limited to articles published after 2000, written in English, and the resulting articles were sorted via most cited. The search string used is “Isolated AND AC/AC AND converter”. The resulting 98 articles were reduced to 86 after removing duplicate articles, and incorrectly returned results such as DC/DC converters and DC/AC inverters.

To further reduce the number of unsuitable articles, a review of the abstracts articles is undertaken, to ensure that each article contained relevant content; namely AC/AC conversion where isolation is realized by a high-frequency transformer. Articles that did not focus on the AC/AC converter itself, but rather focused on a smaller component of the system were removed. Articles that focused on three-phase converters were reviewed for any unique overview on topologies in general, but the benefits of three-phase topologies were not compared to other single-phase topologies. Some articles discussing non-isolated converters were included to show limitations of specific topologies.

After the abstract review, 60 articles remained for the full review. From these articles, key information is recorded to be used in a direct comparison and find the most suitable solution to fulfil the specifications. After articles containing duplicated information and topologies were removed from the review, 13 of the 60 that were read in full, remained.

From the resulting articles, it is clear that three main classifications of AC/AC converters exist as shown in Figure 3. The three main classifications and some specific topologies are discussed in detail in Section 2.3.

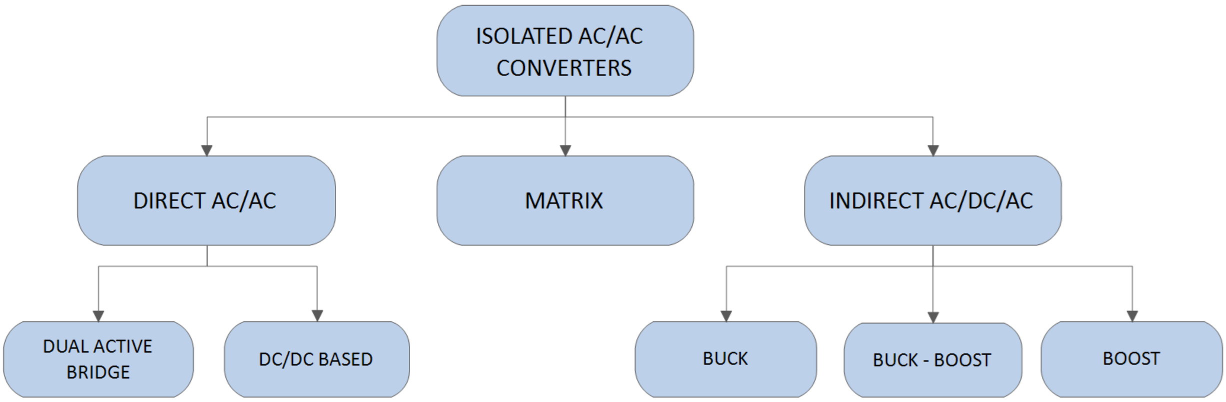

Figure 3: Classification of AC/AC converters

2.3 Methods of AC/AC Conversion

To compare the methods of AC/AC conversion, the following criteria were used: the ability to perform frequency conversion, whether the method incorporated high-frequency isolation, number of stages, voltage conversion range, the use of electrolytic capacitors, and control complexity.

The ability to perform frequency conversion, high-frequency isolation, and the voltage conversion range are all key specifications that the chosen topology must be able to provide. The use of electrolytic capacitors relates solely to lifespan and failure rates, therefore, it is an important consideration. The number of stages and control complexity are included in the comparison as this will affect the overall design complexity and ease of maintenance and repair.

Table 2: Comparison of AC/AC methods

Topology	Frequency Conversion	High Frequency Isolation	No. of Stages	Voltage Conversion	Electrolytic Capacitors	Control Complexity	References
Direct AC/AC	None or Limited	Yes	1	Step Up / Down	No	Low	[13], [37], [14], [38], [15]
Matrix Converter	Limited	No	1	Step Down	No	High	[16], [19], [17], [18]
DC-Link	Yes	Yes	3	Step Up / Down	Yes	Medium	[20], [39], [40], [21]

The results of the comparison are summarized in Table 2, which shows that the DC-Link converter meets the required specification of frequency conversion which neither the direct AC/AC converter nor the matrix converter provides. Further comparison of each topology is undertaken in the remainder of Section 2.3.

2.3.1 *Direct AC/AC*

The direct AC/AC converter is the most commonly used method of AC/AC conversion when voltage conversion alone is required [13]. The most common topology of direct AC/AC converter is the dual active bridge (DAB) converter [14], [15]. Like all direct AC/AC converters, DAB converters do not use a DC-link, but instead, modulate the AC waveform directly using H-bridge configurations as shown in Figure 4.

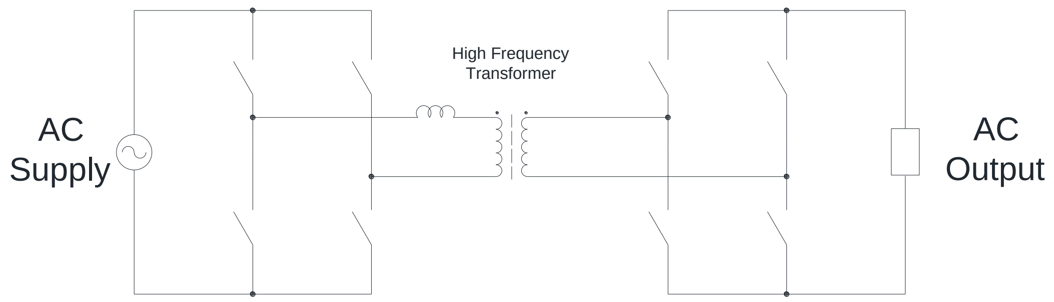

Figure 4: Dual active bridge (DAB) topology

The main disadvantage the DAB converter faces is the inability to perform frequency conversion. This is due to the zero crossings in the input voltage waveform, where no instantaneous power transfer can happen, and due to the lack of energy storage in the converter, this limits the output waveform to the same zero crossings. This also limits the amount of reactive power that can be drawn from the converter, which is further explained in [14].

While this converter is a promising solution to AC/AC conversion, it is only applicable in situations where frequency conversion is not required. One potential solution to this limitation is the matrix converter [16], [17], [18].

2.3.2 Matrix Converter

The matrix converter is a form of AC/AC converter that uses arrays of bidirectional switches to directly convert AC/AC. Matrix converters have the benefit of having the ability to transfer power bi-directionally [19], which makes it an attractive solution for grid-tied converters for renewable energy systems. Three-phase matrix converters are the most popular application, as the constant input power provided by the three-phase supply allows more complex frequency conversion. Single-phase matrix converters such as Figure 5 do not have this constant input power; therefore, the frequency conversion is limited.

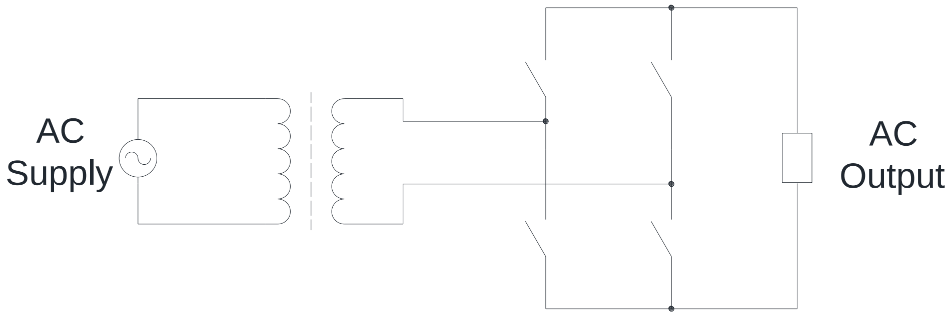

Figure 5: Single-phase matrix converter

Although limited frequency conversion is possible with the single-phase matrix converter, a complex control algorithm must be used, and it is limited to multiples of the fundamental frequency due to the zero crossings of the input waveform when a single-phase input is used [18]. This is not suitable, as changing from 50 Hz to 60 Hz is the most commonly required frequency conversion for a shore power converter. The most significant disadvantage of the matrix converter is the voltage conversion ratio, which is limited to a maximum of 0.86. This shows that the matrix converter is fundamentally limited to applications where the input voltage is greater than the required output voltage, and no large voltage conversion is required [16].

The matrix converter is a promising solution to AC/AC conversion for industrial equipment such as variable speed drives, and simple grid-tied converters, as it boasts an extremely simple topology with no passive components other than input and output filters. The lack of a DC-link improves the lifespan of the converters, as no electrolytic capacitors are required. However, the complexity of the control algorithms [19], the limitations on voltage conversion, and extra stages required to incorporate features such as high-frequency isolation make it unsuitable for many applications [16]. One method of AC/AC conversion does not include any of these limitations, the DC-Link converter.

2.3.3 *DC-Link Converter*

DC-link converters, also known as indirect AC/AC converters, are primarily used when both voltage and frequency conversion is required. The main advantage of a DC-link converter is the decoupling between the two AC stages, which allows for independent current control of the input and output [20]. This solves the limitation with reactive loads that the direct AC/AC converter experiences in [14], and allows for full frequency conversion which is a significant limitation of the direct AC/AC and the matrix converters.

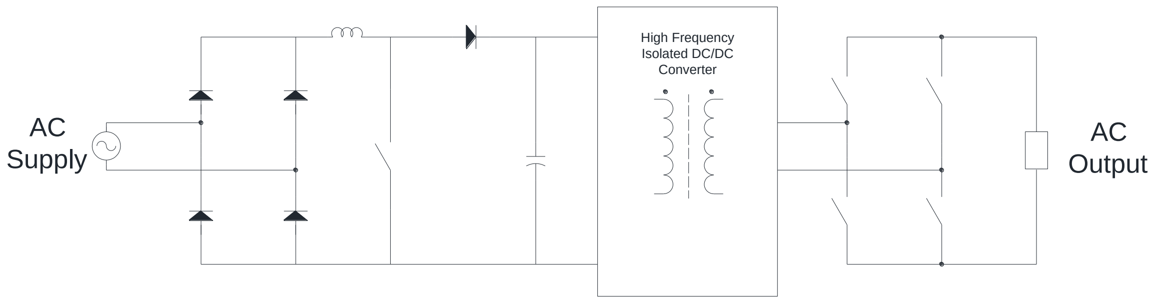

Figure 6: DC-link converter

The most common topology is the three-stage approach which uses a full bridge rectifier PFC stage, DC/DC converter, and output inverter [14]. When isolation is required, this can be incorporated into the DC/DC converter as a high-frequency transformer as shown in Figure 6, or as a mains frequency transformer placed before the rectifier. The main disadvantage of this topology is the multiple stages required to form a complete system, which adds additional components and increases points of failure, especially due to the use of DC-link capacitors [19].

The DC-link converter relies heavily on the use of a full-bridge rectifier with a capacitive filter, which causes a non-sinusoidal current to be drawn from the grid supply. This introduces the need for active PFC, which is normally realized by a boost PFC converter, as described in [21]. Active PFC dynamically shapes the input current to match the waveform of the input voltage, thereby reducing the harmonic content and improving the power factor.

This boost PFC stage is then followed by a DC/DC stage that regulates the DC voltage to provide a stable supply for a DC/AC inverter. The DC-link requires multiple large electrolytic capacitors to smooth the rectified AC voltage and helps filter any high-frequency ripple created by the switching of the DC/DC stage [21]. These electrolytic capacitors are a significant disadvantage of DC-link converters, as they can have a short life span, and take up a significant amount of space.

However, in common with the matrix converter, the use of a three-phase input can greatly reduce the size of the electrolytic capacitors needed. These are important factors in the design of a converter. Therefore, significant research attention has been placed on reducing, or completely removing electrolytic capacitors, usually by much more reliable DC film capacitors, at the expense of volume and weight. Due to the significant increase in volume and weight when using film capacitors, for a shore power application, long life electrolytic capacitors are preferred.

2.4 AC/AC Conclusion

From the AC/AC literature review, summarized in Table 2, it is apparent the DC-link converter is best suited to the specifications necessary for a shore power converter in terms of frequency conversion, wide voltage conversion range, and high-frequency galvanic isolation.

Although it is clear a DC-link converter is required, the common three-stage approach still has the disadvantages of multiple stages, the use of electrolytic capacitors and increased points of failure. To find a more suitable approach to a DC-link converter, a secondary literature review is then conducted to find a suitable AC/DC stage for the DC-link converter, as this is the key area for improvement.

2.5 AC/DC Literature Review Method

The purpose of the second literature review is to identify a suitable topology to perform the AC/DC conversion required for the DC-Link converter. AC/DC topologies are the focus of this review, as the disadvantages of multiple stages, reduced efficiency, and use of electrolytic capacitors all lie within the AC/DC stage.

Since the AC/DC converter must provide galvanic isolation and active PFC, the search string used is "(((((Isolated) AND AC/DC) AND PFC) NOT AC/AC) NOT DC/AC)". The search is then limited to articles published after 2000, written in English, and sorted by most cited. This resulted in 136 returned articles, which were first filtered by title, removing incorrectly returned results such as DC/AC converters, and duplicate articles. This left 124 articles, the abstracts of which were reviewed.

The abstract review is conducted to further understand the content of the articles, and articles that weren't deemed relevant were removed from the review. Removed articles included those in which the topology could not integrate high-frequency isolation, articles that focused on adapting existing single-phase topologies to three-phase applications, and articles that focused on a specific aspect of a converter, such as the control system if they provided no insight into the overall converter.

This left 62 articles for a full review, of which a classification of the topologies is created in order to categorize the articles, as seen in Figure 7.

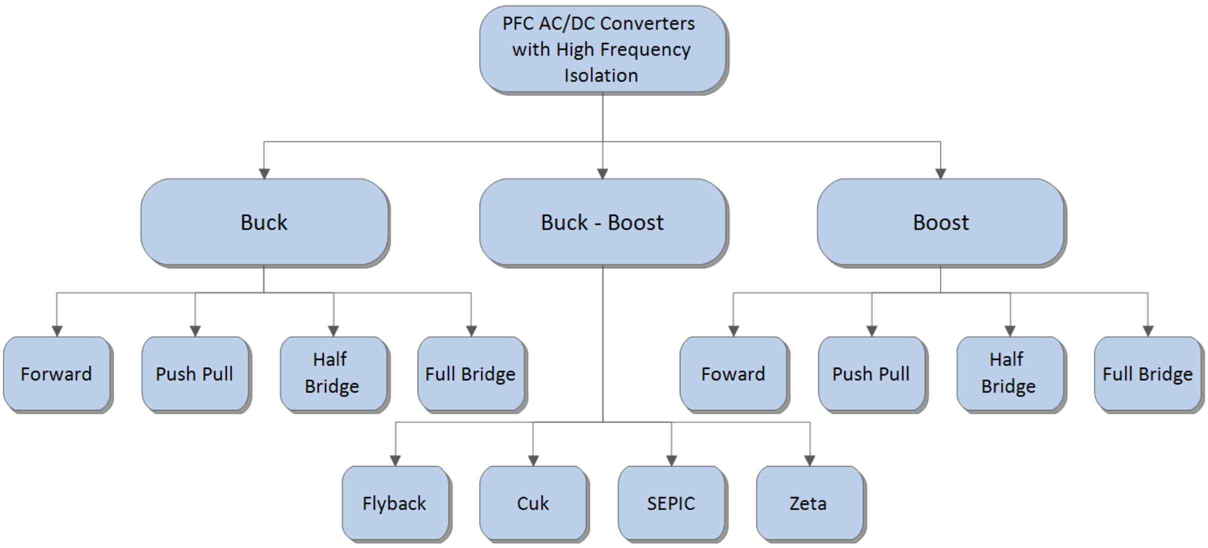

Figure 7: Classification of AC/DC converters

Since the DC-link topology requires a large input voltage range, only AC/DC topologies that fell within the buck-boost classification were selected. Single-stage topologies were also preferred as they have a clear advantage over the two-stage approach, due to the reduced size and number of components [8], [22]. Due to the power level requirements and the need for scalability for use in a shore power converter, AC/DC converters that have both continuous input and output currents are preferred. Due to these findings, the resulting 62 articles were again filtered using the criteria of single-stage, buck-boost classified AC/DC converters. This resulted in 17 articles to be used directly in the comparison

2.6 Methods of AC/DC Conversion

A comparison is undertaken on single-stage, buck-boost classified AC/AC topologies discovered in the review. Terms of comparison included the use of an input rectifier, the nature of input and output current waveform, number of components, number of active switches, and efficiency. Comparison results are given in Table 3.

Table 3: Comparison of single-stage isolated buck-boost AC/DC topologies

Topology	Input Rectifier	Input Current Form	Output Current Form	Number of Components	Number of Switches	Efficiency	References
Flyback	Full bridge or bridgeless	Discontinuous	Continuous	10 – 15	1 – 2	85 - 91%	[22], [23], [24], [41]
SEPIC	Full bridge	Continuous	Discontinuous	10	1	91.5%	[26], [27], [28]
Zeta	Full bridge	Discontinuous	Continuous	12	1	85 – 94%	[25], [26]
LLC Resonant	Full / half bridge	Discontinuous	Continuous	15 - 20	2 – 4	85 – 90%	[30], [29], [42], [43]
Bridgeless Isolated Converter	Bridgeless	Continuous	Continuous	9	1	90 – 98%	[8], [31], [44], [45]

2.6.1 Flyback

The flyback converter is most commonly used in DC/DC converters and low power AC/DC converters [22], which usually have low output voltage. The main disadvantage of the flyback converter is the discontinuous input current, due to the switch in series with the transformer. This creates higher peak currents and higher EMI levels which do not scale well to higher power levels.

Conventional flyback converters require a pre-regulator to perform active PFC to improve harmonic content and power factor to suitable levels to meet international standards, but the dual conversion method increases the number of components, size of the converter, and control complexity [22]. Extra stages of conversion also reduce operating efficiency.

To improve efficiency and reduce the size of the conventional two-stage flyback converter, single-stage bridgeless flyback converters are introduced in [23] and [24]. Although these converters claim to be single-stage, in reality, they are two separate flyback converters operating in parallel, with each separate converter operating for one half of the input line cycle. This is an inefficient way to form a single-stage converter as the components are only utilized 50% of the time. These converters are also limited to discontinuous conduction mode (DCM), or critical conduction mode (CRM) to be able to perform PFC. This is a big limitation in scaling to higher power levels, as operating in DCM or CRM cause higher peak currents and more EMI than operation in continuous conduction mode (CCM).

2.6.2 Zeta

Similar to the flyback converter, the zeta converter is a commonly used DC/DC converter for low power applications. The zeta converter also has a discontinuous input current and continuous output current and must operate in DCM or CRM to perform PFC [25]. To perform PFC without operating in DCM or CRM, a multi-stage approach can be taken similar to the flyback converter, where a PFC pre-regulator such as the boost converter is used [26]. The zeta converter uses a full bridge rectifier on the input, and therefore conduction losses are increased, reducing the efficiency. Therefore, the zeta converter has similar disadvantages to those outlined for the flyback converter.

2.6.3 SEPIC

The Single Ended Primary Inductance Converter (SEPIC) is a typical buck-boost classified DC/DC converter that can be repurposed into an AC/DC converter using a full-bridge rectifier or bipolar switching methods. Typically, the SEPIC is operated in DCM to provide inherent PFC [27], although as seen in [28], operating in CCM while performing active PFC is possible using more complex control schemes. While the SEPIC has continuous input current, unlike the flyback converter, the output of the SEPIC is discontinuous, which increases the output voltage ripple, requiring larger bulk capacitance to have a steady output voltage.

2.6.4 LLC Resonant

One of the most popular recent topologies is the LLC resonant converter. This converter is usually used as the second stage in the two-stage AC/DC converter, to incorporate high-frequency isolation after a boost PFC stage [29]. Its main advantages are the soft switching caused by the resonant tank, and that it can perform fast voltage regulation to remove the low-frequency output voltage ripple caused by the input waveform and voltage variations created by the boost PFC [29]. Many versions of this topology have been proposed in the literature using different input bridge forms, sometimes replacing the diodes with active switches, or combining with a boost PFC converter to create a single-stage approach as seen in [30]. However, these proposed single-stage converters still perform rectification before the PFC and isolation can be implemented, which increases the number of switches and complexity of the control strategy. As for the flyback and zeta converters, the single-stage LLC resonant converter has a discontinuous input current and operates in DCM to perform PFC. The single-stage LLC resonant converter also has a very high component count for a single-stage approach, although the extra components provide soft-switching which reduces switching losses and stress.

2.6.5 Bridgeless Isolated Converter

The bridgeless isolated converter is the only topology in the literature review that has both continuous input and output current. This continuous output current is provided using series resonant components which give the converter a unique semi-resonant operation, as resonance only occurs when the switch is closed. This is an attractive feature for use at higher power levels, as EMI is reduced, and both input and output ripple currents are reduced.

This also means the filtering effort on both input and output is reduced, decreasing the size and weight needed for filter components. The semi-resonant operation described in [8] does not provide full soft-switching as the resonant circuit in the LLC resonant converter does, although switching losses of the bridgeless isolated converter are still reduced by the resonant operation, as the resonant current falls to zero before the turn-off of the main switch. The lack of a full bridge rectifier on the input reduces conduction losses, and fewer components reduce size and weight while keeping efficiency high. This is claimed to be the first "True Bridgeless" converter, as it eliminates all diodes on the input of the converter, unlike other bridgeless converters which still use input diodes in combination with the active switches [8].

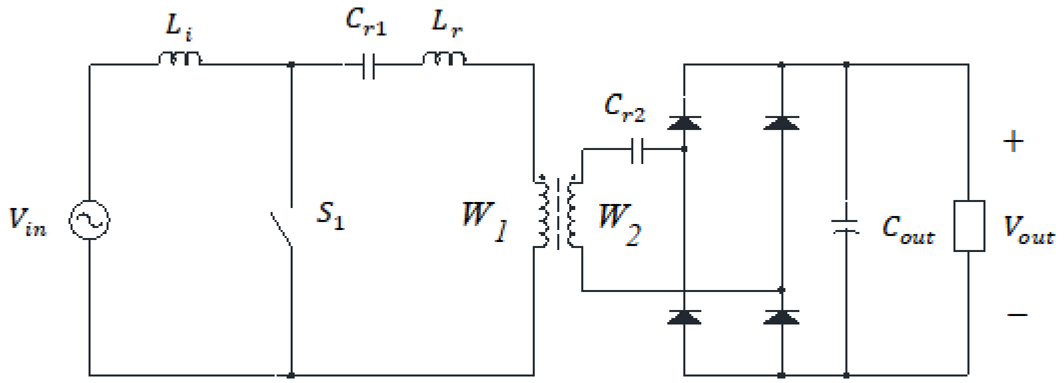

Figure 8: Bridgeless isolated converter [31]

This makes the bridgeless isolated topology one of the most promising topologies found in the literature survey, as it utilizes a single-stage single-switch approach while still being able to perform PFC, AC/DC conversion, and provide high-frequency isolation. Therefore, an in-depth review of the converter is undertaken to explore existing knowledge on the converter and discuss any potential limitations.

As described in [8], the bridgeless isolated converter can accommodate a half-bridge or a full-bridge output rectifier configuration as shown in Figure 9 and Figure 10.

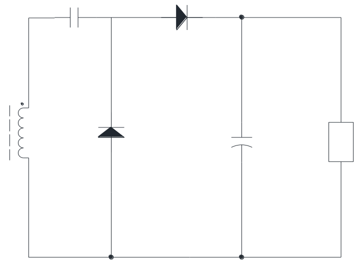

Figure 9: Half-bridge output rectifier

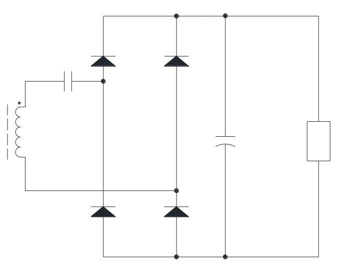

Figure 10: Full-bridge output rectifier

This rectifier is uniquely used in the bridgeless isolated converter, as all diodes are utilized across the entire switching period during any input voltage polarity. This is a large benefit compared to standard AC/DC converters where there is a dedicated full-bridge input rectifier, and then multiple diodes used in the high-frequency stage of the AC/DC converters. As discussed in [31] the full-bridge output rectifier is preferred for the bridgeless isolated converter as this allows for continuous output current. Due to the benefits of the full-bridge rectifier, it will be used for all further analysis. The proposed topology utilizing the full-bridge output rectifier is shown in Figure 8.

The operation of the bridgeless isolated converter can be simplified into two states when operating in a steady-state condition, as the operation is the same regardless of input voltage polarity [8]. The two states of operation are when the switch is closed (t_{on}) and when it is open (t_{off}). During t_{off} the input current flows in a single current loop through the input inductor, series resonant tank, and the transformer. During this period, no resonant operation occurs, and the resonant capacitors charge up to store energy, which gets discharged during the resonant operation. This operation is true for either input polarity. This current also supplies the load for either input polarity due to the full-bridge output rectifier.

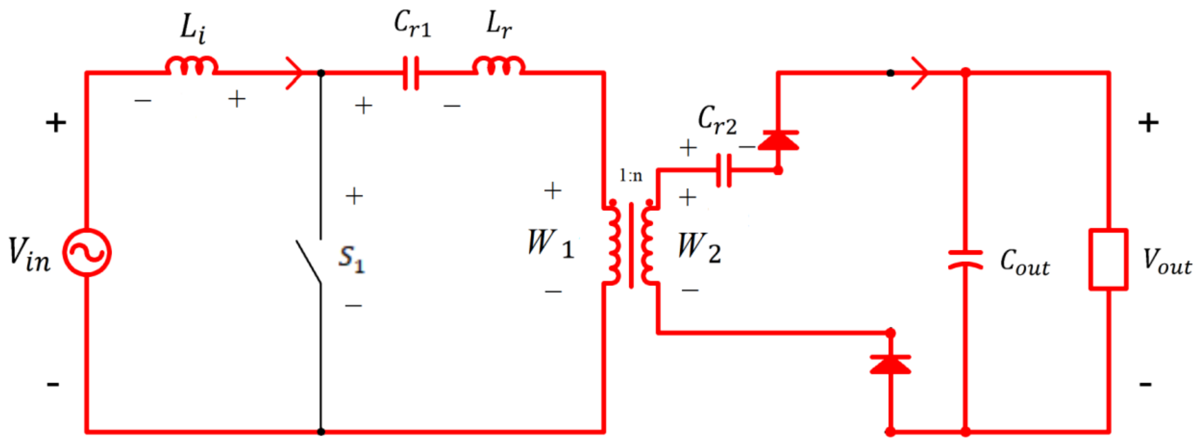

Figure 11: Switch open operation ($\boldsymbol{t_{off}\ period}$)

During t_{on}, two current loops are formed. The first flows from the input, through the input inductor, the switch, and back to the source as shown in Figure 12. This stores energy in the input inductor L_i to allow it to supply the load during t_{off}. The second loop is what provides the bridgeless isolated converter with its unique semi-resonant operation, as the energy stored in the resonant capacitors C_{r1} and C_{r2} begins to resonate with the resonant inductor L_r, creating the second current loop which, due to the full-bridge output rectifier, will also supply the load during either input polarity. This resonant current is what allows the transformer to operate with no DC bias, as the resonant current provides volt-second balance at the switching frequency. This also provides the bridgeless isolated converter with the unique continuous output current while keeping a continuous input current. Other converters such as the SEPIC [28] with a continuous input current, usually have a discontinuous output current. Therefore, the output capacitor size needs to be larger, as the output capacitor is solely relied on to supply the load for half of the switching period. Since the bridgeless isolated converter has continuous input and output currents, the filtering effort on both the input and output is reduced. This gives a unique advantage over other converters. Although reducing filter size is important, it is often not considered in the literature. The resonant operation also demonstrates the unique use of the full-bridge rectifier, where all diodes are utilized across one switching period. This is unlike other converters, where two or more diodes are unused for one half of the AC input line cycle.

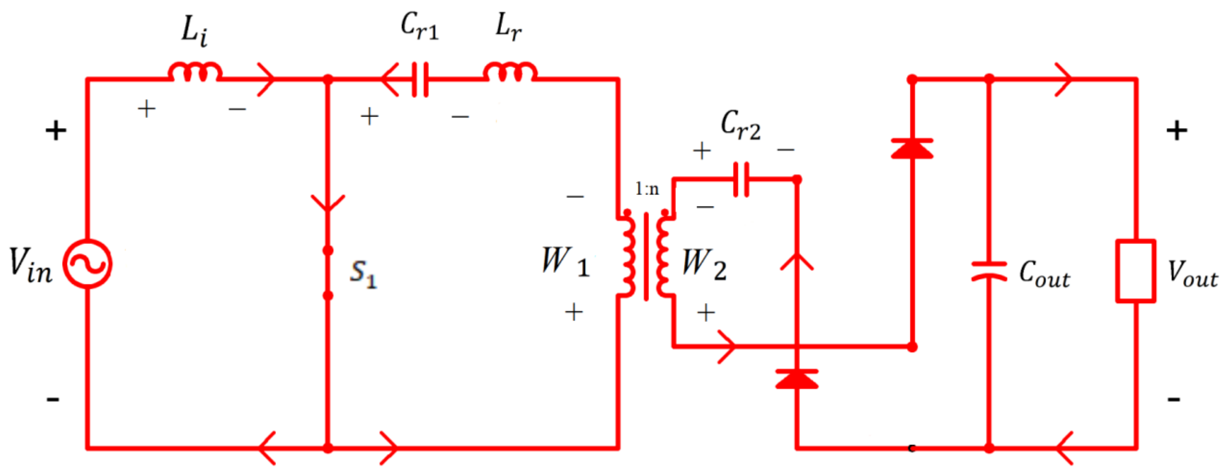

Figure 12: Switch closed operation ($\boldsymbol{t_{on}\ period}$)

One issue outlined in existing literature for the bridgeless isolated converter is the potential for an overvoltage of S_1 during the opening of the switch. During the opening of the switch, the resonant inductor L_r must rapidly change from zero current to the current magnitude of the input inductor L_i. This is caused by the removal of the existing current path for L_i when the switch begins to open, and the current begins to flow through the inductor L_r. The rate of change of the current through the inductor L_r has a dependency on the switching speed of S_1. To decrease switching losses, it is desired that this switching speed is as fast as possible. Therefore, and in accordance with Lenz's Law, a high transient overvoltage can occur across S_1. Since the resonant inductor is relatively small, the overvoltage can be clamped using bidirectional TVS diodes, although as the power level of the converter is increased, a significant reduction in efficiency may be experienced. Therefore, a more efficient method of controlling the overvoltage across S_1 is desirable.

The resonant circuit is arguably the most crucial part of the design of the bridgeless isolated converter, as this is what provides the resonant operation during t_{on}. In [31], the well-known equations to define the resonant frequency from the L and C components are shown, as well as the consideration of two series capacitors as part of the resonant tank. However, as stated in [31], these individual component values have a larger effect on the circuit than just defining the resonant frequency. For example, the resonant inductor L_r must have both a minimum and maximum value if it is to be derived from the transformer's leakage inductance, as there is a practical limit to how low the leakage inductance can realistically be. The overvoltage created by L_r that can appear across S_1 also needs to be taken into consideration, as this is directly dependant on the size of the inductor, and the current flowing through it, and therefore determines a maximum inductance.

The resonant capacitor C_r also has a larger effect on the operation of the converter than just providing resonant operation. During each switching cycle, the resonant capacitor charges during the switch open period, and discharges during the resonant switch-off period. This charging and discharging create a ripple voltage on the resonant capacitor, the amplitude of which is proportional to the value of the resonant capacitor itself. Therefore, to avoid adding extra voltage stress to the switch S_1, the ripple should be restricted to a maximum value when designing the resonant circuit. The second problem introduced by the resonant capacitor value is the charging and discharging time during each change of input polarity. The capacitor takes a non-negligible amount of time to discharge and charge before and after the zero crossings of the input waveform. This period that is taken to charge affects the ability to perform active PFC.

2.7 Conclusion

From the review of existing AC/AC methods, it is discovered that to meet all the key specifications of a shore power converter, such as high-frequency isolation, frequency conversion, wide input voltage range, and active PFC, a DC-link converter is required.

Although DC-link converters exist commercially today, there are many drawbacks and limitations. The most significant are the multiple stages of conversion required to incorporate high-frequency transformers and the input full bridge rectifier which adds significant conduction losses.

The bridgeless isolated converter proposed in [8] has many advantages over existing AC/DC topologies, as it can perform active PFC and AC/DC conversion, while providing isolation through a high-frequency transformer using a single switch, single-stage, bridgeless design. While this converter shows promise, there are still limitations and areas lacking research before it can be utilized for shore power converter applications. One key area that needs further research is the design and implementation of the resonant circuit. The components that make up the resonant circuit affect multiple aspects of the operation of the converter, and there are limitations on the combination of component values that can be used.

A design procedure that considers these limitations and shows a method to optimize the resonant circuit does not yet appear to exist. In [31] it is stated that "for optimal circuit behaviour Cr and Lr need to be designed properly although they do not have direct influence". However, a procedure on how to properly design these components is not presented. This thesis will investigate and develop a design procedure that considers these limitations, to add to the existing knowledge of the bridgeless isolated converter and make future converter design simpler. The overvoltage of the switch S_1 will also be briefly addressed, although analysis of this issue has already been investigated in existing literature [31], [32]. A method of limiting this overvoltage will be implemented for the prototype circuit developed for this research.

2.8 Research Questions

With the above gaps in knowledge identified, the following research questions are developed.

- Is the bridgeless isolated converter topology operating with active power factor correction suited to the power levels required for a shore power converter?

- Can a detailed design procedure for the resonant components improve the operation of the bridgeless isolated converter?

Chapter 3

Design

3.1 Introduction

In Chapter 2 the bridgeless isolated converter was introduced. In a single-stage and using a single active switch, this can perform active PFC, AC/DC conversion, and provide galvanic isolation. This makes it suited to shore power converter applications. However, the review of this converter showed a gap in existing literature regarding a design procedure for the resonant components. These resonant components affect multiple aspects of the operation of the converter, which makes design a non-trivial task. Therefore, and in this chapter, a design procedure that considers these effects will be developed to produce an optimized resonant circuit for the converter.

This chapter will also detail all other converter design aspects. An initial assumption is made that the input current is sinusoidal for the sake of the design procedure. Active PFC is added to the design at a later stage, and it is shown this does not affect the design procedure accuracy.

The design of the entire converter is detailed in this chapter, although there is a significant focus on the design procedure of the resonant circuit. Initially, and to allow the design of the resonant components, the conversion ratio of the converter is derived, and the input inductor is designed, as these parameters are required in the design procedure. The design procedure for the resonant circuit is then outlined, and the specific design is undertaken. Finally, the output capacitor is designed, resulting in complete design of the bridgeless isolation converter.

3.2 Design

The voltage conversion ratio of the bridgeless isolated converter can be derived by applying the volt second rule to the input inductor L_i. The conversion ratio for the half-bridge version has been derived in previous literature. The conversion ratio for full-bridge version differs and is shown in [31]. However, the derivation of this conversion ratio is not shown. Therefore, the conversion ratio is derived in Section 3.2.1 and is based on the volt-second rule. From expressions developed during the derivation, a design procedure for the converter resonant components is later derived.

3.2.1 Conversion Ratio

The volt-second rule requires the area underneath the voltage waveform across the input inductor L_i to be equal for both the on-time (t_{on}) and the off-time (t_{off}) of S_1. Figure 11 shows that during t_{off}, the input inductor voltage (V_{L_i}) must be equal to the difference between the input voltage and the switch voltage ($V_{S_1} - V_{in}$). The time that the switch is open is considered t_{off} which is equal to $(1 - D) * t_s$, where t_s is the period of the switching frequency, and D is duty cycle. The time that the switch is closed is considered t_{on} which is equal to $D * t_s$. As seen in Figure 12, during t_{on} the input inductor voltage is equal to the input voltage, due to Kirchhoff's law. The volt-second rule can be expressed as:

$$V_{L_i\,(t_{on})} * t_{on} = V_{L_i\,(t_{off})} * t_{off} \tag{3.1}$$

Substituting the inductor voltages for expressions in terms of input and switch voltage into (3.1) gives the volt-second rule in terms of the switch voltage as shown in (3.2)

$$V_{in} * t_{on} = \left(V_{s1\,(t_{off})} - V_{in}\right) * t_{off} \tag{3.2}$$

The switch voltage can be derived from Figure 11 and using Kirchhoff's law to give the switch voltage in terms of the transformer winding voltage and the resonant capacitor voltage as shown in (3.3).

$$V_{S_1\,(t_{off})} = V_{C_{r1}} + V_{W_1} \tag{3.3}$$

Since the transformer separates the two resonant capacitors, the primary and secondary voltages need to be expressed in terms of output voltage, resonant capacitor voltage and winding ratio to be able to derive the conversion ratio. Therefore, the switch voltage can be expressed in the same terms by substituting the transformer winding voltage V_{W_2} into V_{W_1}.

$$V_{W_2} = V_{C_{r2}} + V_o$$

$$V_{W_1} = \frac{V_{W_2}}{n} = \frac{V_{C_{r2}} + V_o}{n}$$

The switch voltage can then be derived using Kirchhoff's law and substituting in V_{W_1} into (3.3) gives (3.4).

$$V_{s1\,(t_{off})} = V_{C_{r1}} + \frac{V_{C_{r2}} + V_o}{n} \tag{3.4}$$

It is apparent in Figure 12, during t_{on} the sum of the voltages across the two resonant capacitors must be equal to the output voltage scaled by the turns ratio and is shown mathematically in (3.5). This is true for both t_{on} and t_{off} as shown in [8].

$$V_{C_r} = V_{C_{r1}} + \frac{V_{C_{r2}}}{n} = \frac{V_o}{n} \tag{3.5}$$

Therefore substituting (3.5) into (3.4) results in the final switch voltage expression in terms of the output voltage.

$$V_{S_1\,(t_{off})} = \frac{2V_o}{n} \tag{3.6}$$

Substituting (3.6), and the expressions of t_{on} and t_{off} in terms of D into the volt-second rule for the input inductor given by (3.2) provides the desired form of the conversion ratio.

$$\frac{V_o}{V_{in}} = \frac{n}{2(1-D)} \tag{3.7}$$

This conversion ratio can then be used to calculate the duty cycle D required for specific input and output voltages. The expressions derived in the derivation of the conversion ratio are also used in the resonant design procedure, and therefore are relevant.

3.2.2 Input Inductor

The design of the input inductor is based on allowable input ripple current, as set by the inductance. However, this is not the only factor that needs consideration, as the physical size is also important. The inductance can be calculated using (3.8), derived in [31].

$$L_i = \frac{V_o}{2n\Delta I_{L_i} f_s} \tag{3.8}$$

To give the converter a wider operation in the boost region, due to the specified minimum input voltage being more than four times lower than the specified output voltage, the transformer winding ratio is chosen to be 1.25. To keep electromagnetic interference (EMI) emissions within acceptable limits and reduce the amount of input and output filtering required, the switching frequency is chosen to be 75 kHz. This has a second harmonic of 150 kHz, which is an important limitation in EMI frequencies as many electromagnetic compatibility (EMC) standards such as CISPR and IEC 61000 classify disturbance levels in the ranges of 0 – 150 kHz and 150 kHz – 150 MHz. Therefore, it is beneficial to keep all EMI within one classification range, while still taking advantage of high-frequency operation [32].

The allowable input inductor ripple current ΔI_{L_i} has been chosen to be 35% of the maximum input current. This is to reduce the physical size of the inductor, as lower ΔI_{L_i} values increase the physical size. Due to this relationship, a higher ΔI_{L_i} is preferred, while keeping the converter in continuous conduction mode. The value of the ripple current can be calculated using (3.9), using the minimum input voltage of 90 V, as this is where maximum input current occurs.

$$\Delta I_{L_i} = \delta \, \frac{P_{in}}{V_{in}} \tag{3.9}$$

Using δ as the previously defined maximum percentage of 35%, the inductor ripple current is calculated to be $\Delta I_{L_i} = 7.77A$ using (3.9). Using this ripple current, the inductance of L_i can be calculated using (3.8). Substituting the switching frequency, output voltage, winding ratio, and ripple current which have been previously derived into (3.8) gives an inductance L_i of $260.8\ uH$.

3.2.3 Switch Implementation

Due to the lack of a rectifier on the input, the main switch S_1 is required to conduct bidirectionally, and with either AC input voltage polarity. This is realised using two MOSFETs connected in a common source configuration to allow controlled bidirectional conduction, as seen in Figure 13.

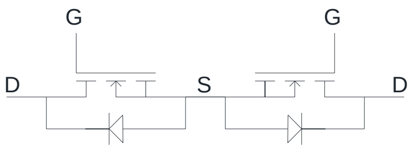

Figure 13: Anti-series MOSFET configuration

While this utilizes two MOSFET packages, they still form a single switch which is controlled by a common gate drive. This reduces control complexity, as a single isolated gate driver can be used. MOSFETs are chosen to implement the switch as they are faster switching devices than IGBTs, and therefore can operate at higher frequencies.

3.2.4 Resonant Circuit Design Procedure

The resonant circuit design procedure needs to consider three key parameters:

1. Resonant frequency, f_r
2. Resonant capacitance, C_r
3. Resonant inductance, L_r

While it is simple enough to choose any two of these parameters and calculate for the third, this does not provide an optimal resonant circuit, as the effects of these components on the rest of the converter have not been considered. To properly design these components, the circuit needs to be simplified to show only the components that have a direct effect on the resonant frequency. After simplification, the following steps can then be used to give an optimized resonant circuit.

1) Firstly, the resonant frequency must be calculated. Since resonance is only achieved during t_{on}, the switching frequency and the duty cycle both determine the limitations in the selection of the resonant frequency.

2) Secondly, the minimum resonant capacitance must be calculated. This can be calculated based on the maximum ripple voltage across the resonant capacitor, as this ripple voltage directly affects the switch voltage.

3) Thirdly, the minimum resonant inductance can be set based on the minimum achievable leakage inductance of the transformer, as this is a practical limitation of the transformer design.

4) Finally, with both the minimum resonant capacitance and minimum resonant inductance calculated, the suitable range of both C_r and L_r can be calculated using the designed resonant frequency. From this range, a realistic combination of the two can be selected to provide the resonant circuit.

This design procedure results in an optimized range of the resonant components L_r and C_r, from which suitable values can be chosen to provide resonance at the desired resonant frequency.

Simplifying the resonant circuit

In the case of the bridgeless isolated converter, the resonant operation is only achieved when the switch is closed. The current path for the resonant current is shown in Figure 14.

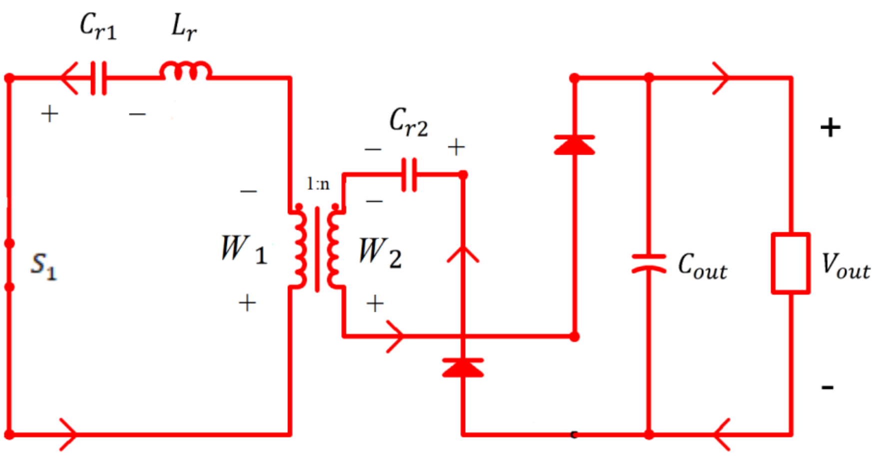

Figure 14: Resonant current path when $\boldsymbol{S_1}$ is closed

The resonant current I_r flows through the resonant components L_r, C_{r1}, C_{r2}, and also the magnetising and leakage inductance of the transformer L_m and L_{lk}, and the load R_{load}.

The equivalent resonant circuit when the switch is closed is shown in Figure 15. The resonant circuit can be reduced to show only the components that have a direct effect on the resonant frequency so that the resonant frequency calculation can be simplified. Through the reflection of the DC load resistance to the AC side of the rectifier as described in [33], the rectifier can be eliminated from the circuit, as this allows the resonant circuit to be simplified. The transformer can then be simplified into the magnetizing and leakage inductances, and secondary side impedances can be reflected to the primary side.

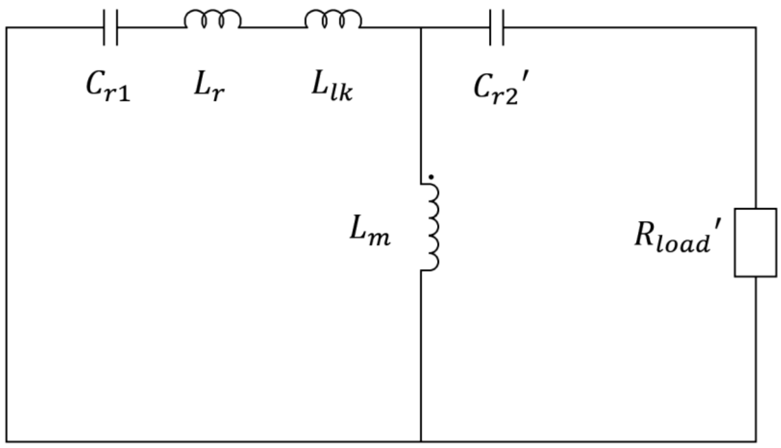

Figure 15: Equivalent resonant circuit

The mutual inductance of the transformer seen in Figure 15 can be removed from the equivalent circuit as L_m is in parallel with L_r , and since L_m is orders of magnitude higher than the resonant and leakage inductors, it does not affect the resonant frequency during t_{on} [8]. Although this does not have a direct effect on the resonant frequency during t_{on}, L_m can create an additional resonance at a much lower frequency, although this does not have an operational effect on the converter, and can be sufficiently damped [31].

However, the leakage inductance L_{lk} of the transformer does need to be considered, as it is much smaller than L_m, and therefore has a direct influence on the resonant frequency of the circuit. Since L_r is also much smaller than L_m, either a series combination of L_r and L_{lk} can be used to form the resonant inductor, or if properly designed, the resonant inductor can be derived solely from the transformer leakage inductance L_{lk}. Therefore, for further analysis, the leakage inductance of the transformer is utilized as the resonant inductor L_r.

Since L_r is volt second balanced during t_{on} only, it does sustain any net voltage during either t_{on} or t_{off}. Therefore, the resonant inductor voltage is not relevant for the circuit analysis.

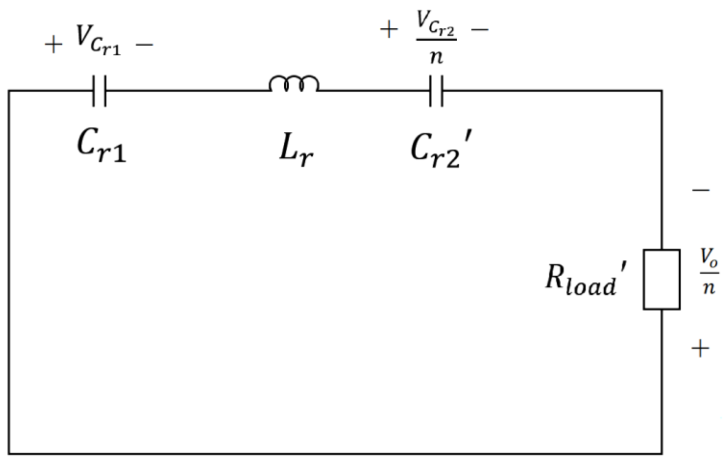

Figure 16: Simplified equivalent resonant circuit

The two remaining resonant capacitors can be combined in series as a single capacitance to make calculations easier, although the individual capacitors that comprise C_r must consider the transformer turns-ratio when calculating total capacitance. As seen in Figure 16, the output voltage polarity is reversed due to the full-bridge rectifier, as this equivalent circuit must still satisfy Kirchhoff's law.

After the above circuit analysis, the simplified equivalent resonant circuit shown in Figure 17 can be used to calculate the values for the resonant circuit.

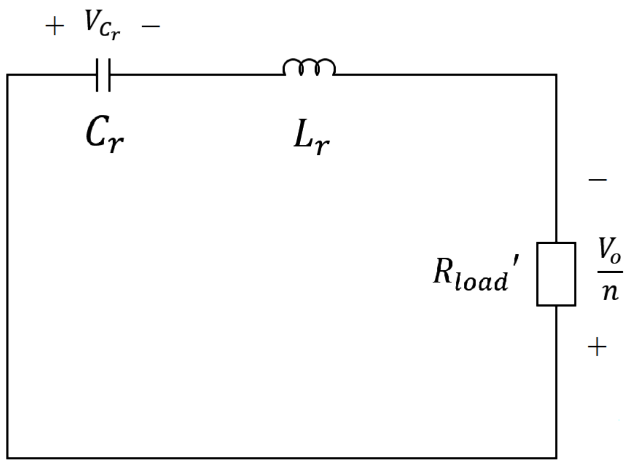

Figure 17: Final simplified equivalent resonant circuit

As shown in Figure 17 the resonant tank of the bridgeless isolated converter is an LC resonant circuit. Therefore, the well-known LC resonant frequency equation (3.11) can be used to calculate the L and C components for a given frequency. Since C_r comprises two resonant capacitors in series separated by the transformer, the total resonant capacitance must consider the winding ratio.

Therefore the total capacitance can be calculated using (3.10) derived in [31], and then substituted into (3.11).

$$C_r = \frac{1}{\frac{1}{C_{r1}} + \frac{1}{C_{r2}n^2}} = \frac{C_{r1} * C_{r2}n^2}{C_{r1} + C_{r2}n^2} \tag{3.10}$$

$$f_r = \frac{1}{2\pi\sqrt{L_r C_r}} \tag{3.11}$$

Design of Resonant Frequency

For the bridgeless isolated converter, the resonant operation only occurs during t_{on}, which must be sufficiently long to allow a half cycle of the resonant frequency to be completed, as shown in Figure 18. Therefore, the resonant frequency is dependent on the switching frequency and, thus t_{on}. The resonant frequency is also affected by whether the switching frequency is constant or variable, as this changes the relationship between the switching frequency and t_{on}.

Initially, the bridgeless isolated converter is proposed to operate with a variable switching frequency, as suggested in [8]. In later literature [31], a comprehensive comparison is made between variable switching frequency and constant switching frequency showing that although the variable switching frequency has small benefits in terms of efficiency (approximately 0.3%), the size required of the magnetics is much larger than required for a constant switching frequency. Therefore, the design will use a constant-frequency, variable on-time control method. To operate optimally with a constant switching frequency, the minimum on-time must not be less than half the resonant period to allow the resonant current to return to zero, as shown mathematically in (3.12)

$$D_{min} = \frac{f_s}{2f_r} \tag{3.12}$$

This shows that to have a wide range of duty cycles, the resonant frequency needs to be much greater than the switching frequency, as apparent from the switching diagram Figure 18.

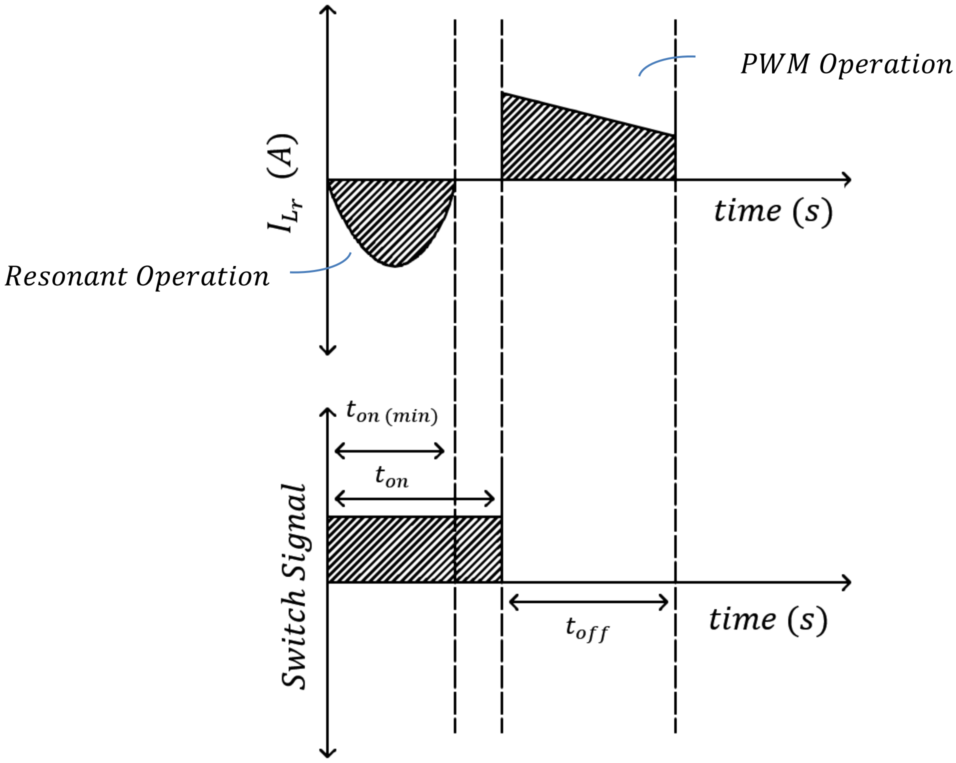

Figure 18: Switching operation

It can be seen in Figure 18 that the resonant current exists for half the resonant period and once it falls to zero there is a small period of zero resonant current, the length of which is dependent on the duty cycle. Since the converter needs to step the peak value of the 300 V_{rms} AC input waveform down to 300 V_{dc}, this sets an upper limit on the range of minimum duty cycles that can be used, and therefore defines a minimum resonant frequency. The duty cycle required to step down the maximum input voltage can be calculated using the conversion ratio (3.7). Substituting V_o of 380 V, n of 1.25, and V_{in} of 300 V into (3.7) gives a duty cycle D of 0.3022.

As calculated, the minimum duty cycle cannot exceed 30% to give the range of voltage conversion required. Figure 19 shows the relationship between the minimum duty cycle and the required resonant frequency. Since a higher resonant frequency would result in higher frequency EMI, it is desirable to keep the resonant frequency within the same testing limits as outlined for the switching frequency. Therefore, a maximum resonant frequency can be set at 150 kHz. With a resonant frequency of 150 kHz, the required minimum duty cycle can be calculated to be 25% using (3.12)

The upper boundary of 30% and a lower boundary of 25% are now set for the acceptable range of minimum duty cycles as shown in Figure 19.

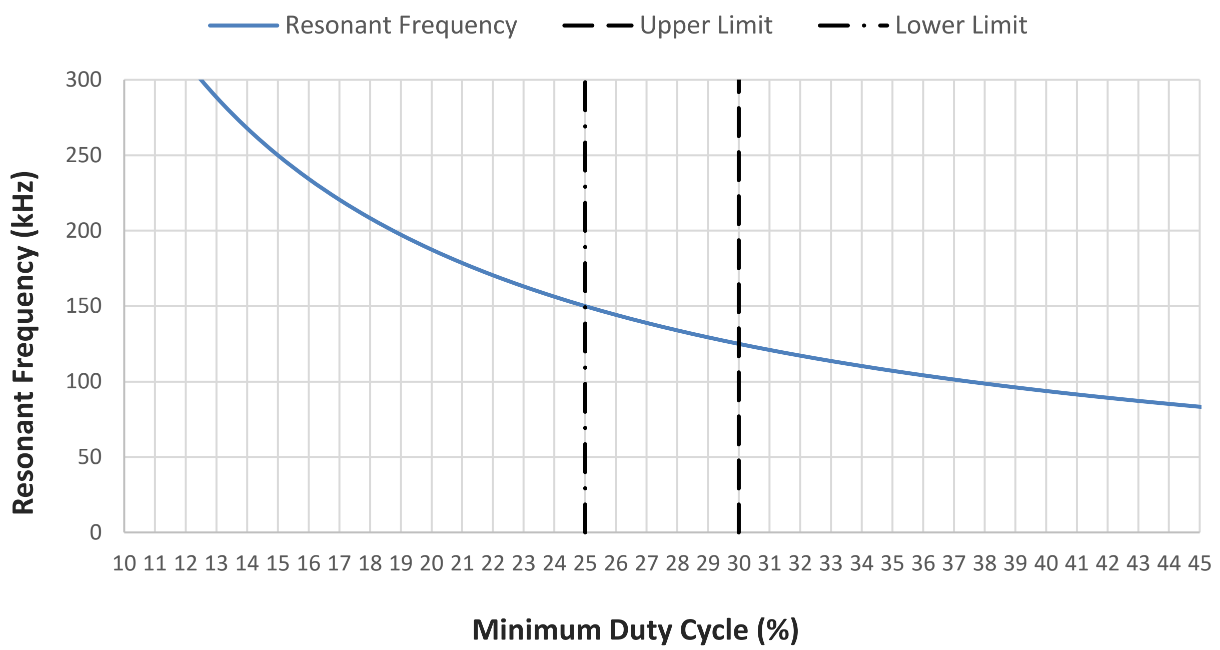

Figure 19: Range of acceptable minimum duty cycles

Since a lower minimum duty cycle gives a wider range of conversion and, therefore, a wider control bandwidth, the minimum value within the range of acceptable minimum duty cycles is chosen, and the resonant frequency is selected as 150 kHz.

Designing resonant capacitance

Now that the resonant frequency has been appropriately designed based on the required operation of the converter, the components that comprise the resonant circuit can be designed. Multiple considerations must be accounted for when calculating values for the individual resonant components. For the resonant capacitor C_r, the two key considerations are the voltage ripple on the capacitor, and the charge and discharge times during the change in AC voltage input polarities as described in Section 2.6. The design of the resonant inductor L_r also needs to consider the maximum overvoltage that it will cause on S_1, and the minimum value possible when considering the series leakage inductance of the transformer.

As described in [31], the equivalent resonant capacitance C_r shown in Figure 17 must charge and discharge to $\frac{V_o}{n}$ and $-\frac{V_o}{n}$ during the positive and negative input voltages respectively. The time required to charge, and discharge is a concern when sizing C_r, as this affects the ability to perform active PFC, and there is no resonant operation during this charge time therefore slightly reducing output power. The charge and discharge time can be reduced but at the cost of a larger capacitor voltage ripple. Due to this effect, the resonant capacitor value should be minimized as much as possible, while keeping the voltage ripple within set parameters. The nature of the capacitor voltage ripple is illustrated in Figure 20, through being superimposed on the average capacitor value during the positive and negative input polarities. This ripple is the most critical consideration in the sizing of the resonant capacitor, as the charge and discharge time can be minimized by modifying the active PFC control system, whereas the ripple voltage can only be controlled by the initial design. This ripple should be limited so that the peak ripple voltage does not exceed the maximum rated switch voltage during t_{off}.

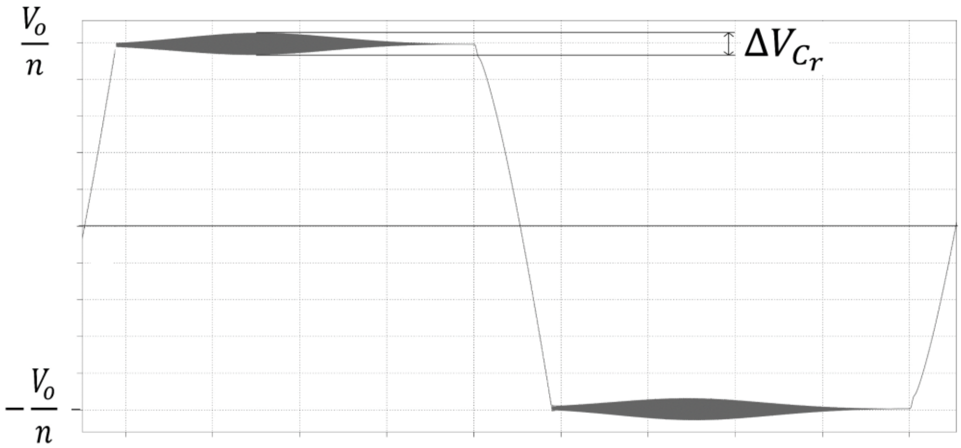

Figure 20: Resonant capacitor voltage

Firstly, the maximum allowable ripple voltage for the capacitor C_r must be set. The switch voltage during t_{off} is calculated assuming zero ripple voltage on the capacitor to provide a starting point for selecting a maximum allowable switch voltage. The switch voltage can be calculated based on the output voltage using (3.6). Using this equation, the average switch voltage can be calculated, as this is the voltage on which the resonant capacitor ripple will be superimposed. This allows the capacitor voltage ripple to be specified for the maximum voltage it will impose across the S_1. Using (3.6), and substituting the desired output voltage, and transformer winding ratio results in an average switch voltage $V_{s1\ avg\ (t_{off})}$ of 608 V.

Since MOSFETs are typically available in 600 V, 800 V, and 1200 V packages, a maximum switch voltage can be selected based on readily available MOSFETs. In this case, a 700 V maximum switch voltage can be set as an upper limit to allow the use of 800 V MOSFETs with a 100 V safety margin, given the maximum operating voltage. A maximum switch voltage of 700 V can be used to calculate the maximum allowable ripple voltage $\Delta V_{C_r\ max}$.

$$V_{S_1\ max\,(t_{off})} = V_{s1\ avg\,(t_{off})} + \frac{1}{2}\,\Delta V_{C_r\,max} \tag{3.13}$$

Using (3.13) and through substitution of $V_{s1\ avg\,(t_{off})}$ and the maximum switch voltage of 700V, the maximum allowable ripple voltage $\Delta V_{C_r\,max}$ is calculated to be 184 V.

A linear approximation of the capacitor ripple can be made using the charge balance rule. Since the resonant capacitor only charges during t_{off}, the capacitor current $I_{C_r\,max}$ is equivalent to the input inductor current I_{L_i}. The maximum input current must be used as this is when the ripple voltage will be at a maximum.

$$I_{C_r\,max\,(t_{off})} = C_{r\,min}\frac{\Delta V_{C_r\,max}}{(1-D)t} \tag{3.14}$$

The duty cycle required for minimum input voltage can be calculated using (3.7). However, the peak of the minimum input voltage must be used, as this is when the input current is at a peak. This duty cycle can then be substituted into (3.14) to solve for the minimum capacitance. Using (3.7) and a minimum input voltage of 90 V, the duty cycle D is calculated to be 79%. Substituting D into (3.14) results in a minimum capacitance of 537 nF.

Design of the Resonant Inductor

A minimum limit for the resonant capacitor has now been designed considering the maximum ripple voltage, and therefore the maximum switch voltage. This allows for the calculation of the resonant inductor. The two considerations for the resonant inductor are the overvoltage created during the turn-off of the switch, and the integration of the leakage inductance. The integration of the leakage inductance is the most critical consideration of the resonant inductor. The main concern is the ability to minimize leakage inductance in the transformer, as this will vary dependant on other parameters of the converter such as power level, voltage specification, and size. Therefore, it is desirable to limit the resonant inductance to an achievable leakage inductance. The overvoltage of the switch caused by the resonant inductance is still an important consideration, but it has been shown in both [31], [32] that the overvoltage can be successfully clamped using TVS diodes for lower power converters, and low loss snubbers for higher power converters. Both methods for clamping this overvoltage will be implemented in the prototype.

Since the integration of the leakage inductance is deemed the more critical consideration, a minimum value of resonant inductance should be set using this consideration. For this research study, the minimum leakage inductance is set at 500 nH, to keep the design of the transformer simple for prototyping purposes.

Selection of Resonant Components from Optimal Range

Now that a minimum resonant inductance and capacitance have been set, an optimal range of resonant values can be calculated for both components. The minimum defined resonant inductance can be used to calculate the maximum resonant capacitance, and the minimum resonant capacitance can be used to calculate the maximum resonant inductance.

Substituting $C_{r\ min}$, and the resonant frequency f_r of 150 kHz into (3.11) provides a $L_{r\ max}$ of 2.1 μH. Likewise, substituting $L_{r\ min}$ and the resonant frequency f_r of 150 kHz into (3.11) provides a $C_{r\ max}$ of 2.25 μF. Therefore a full range for both the resonant capacitor and inductor have been provided, and the range is plotted in Figure 21.

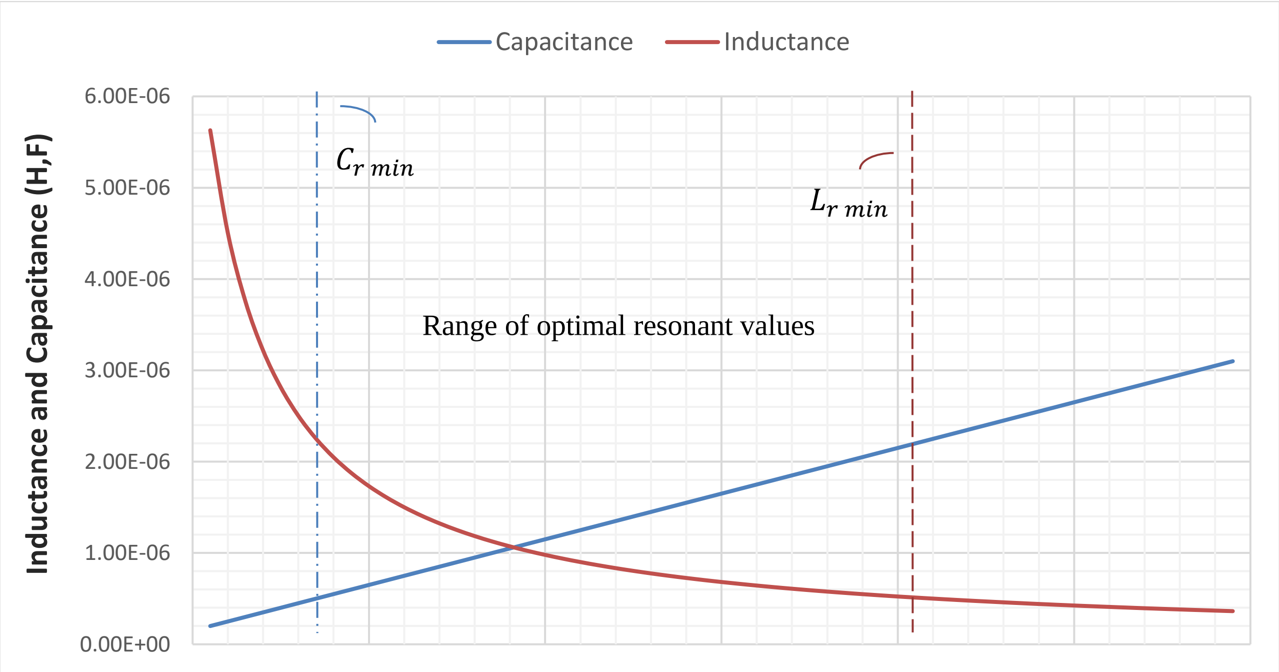

Figure 21: Optimal range of Lr and Cr values for resonance at 150kHz

As seen in Figure 21, there is a wide range of L_r and C_r combinations that will provide resonance at 150 kHz while fitting within the limits designed for the application. Selecting a resonant capacitance of 1 μF as this is a commonly available capacitor value, and using the resonant frequency of 150 kHz, the exact value of the resonant inductor can be calculated by rearranging (3.11) to provide a resonant inductance L_r of $1.126\ \mu H$.

Since the resonant capacitor C_r comprises of C_{r1} and C_{r2}, these two individual capacitor values need to be calculated using (3.10). For a converter with a $1:1$ transformer ratio, this can simply be achieved using two 2 μF capacitors as they are in series, and the total capacitance will be equal to 1 μF. Since the transformer ratio for this converter has been chosen to be $1:1.25$, the individual values will need to be calculated based on this winding ratio. Selecting C_{r2} to be 2 μF so that C_{r1} can be calculated using (3.10) results in a C_{r1} of $1.47\ \mu F$.

3.2.5 Output Capacitors

The output capacitance is defined by the maximum allowable 100 Hz output voltage ripple which is a product of the output rectifier, and the zero crossings of the input voltage. This capacitance must be able to supply the load during zero crossings while keeping the output voltage within tolerance. The equation provided in [31] can be used to calculate the required capacitance

$$C_{out} = \frac{P_o}{2\pi f_{in} V_o \Delta \mathrm{V_o}} \tag{3.15}$$

$$\Delta V_o = \delta * V_o \tag{3.16}$$

Although the value of the output capacitance is not critical, a minimal ripple is preferred to reduce EMI and improve the output voltage stability. While this comes at the cost of extra volume and weight, this capacitance may be reduced further once the specifications of the output stage inverter for the AC/AC converter have been designed. For a ripple voltage of 1% of the specified output voltage, the voltage ripple can be calculated using (3.16) to be $3.8\ V_{pk-pk}$. This can then be substituted into (3.15) along with previously designed circuit parameters, to provide an output capacitance of $4.41\ mF$.

3.2.6 Snubbers

As introduced in Section 2.3, an overvoltage can occur across the switch during the switching off of S_1. This is due to the current in the resonant inductor, i_{L_r}, having to rapidly change from 0 A to i_{L_i}. The magnitude of the overvoltage is defined by the inductance and Lenz's law. Since this rapid change in current is determined by the input current and switching speed of S_1, this overvoltage will scale with the power level of the converter. This shows that the overvoltage needs to be appropriately addressed for the power level of the converter.

As shown in [31], an active snubber is the preferred method for limiting this overvoltage, due to excessive power loss when passive snubbers are used. While this is more complicated than a passive snubber, the advantages in efficiency are desired. Due to this, an active snubber is implemented in the prototype as seen in [31].

3.3 Final Converter Design

Now that each component of the bridgeless isolated converter has been designed, the design can be modelled, simulated and verified. The final design showing the main components in the circuit and their values is shown in Figure 22.

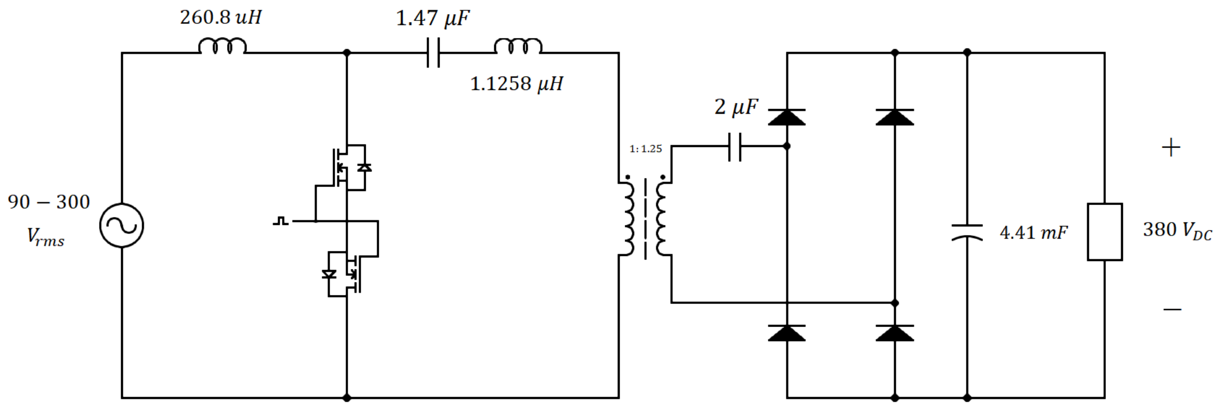

Figure 22: Final design of the bridgeless isolated converter

Chapter 4

Simulation

4.1 Introduction

In this chapter, the design approach in Chapter 3 will be verified through simulation. In addition, the control system for the isolated bridgeless converter will be developed and tested. For these purposes, the software packages MATLAB, Simulink, and PLECS will be used. The advantages of PLECS include allowing for the quick simulation of power electronic circuits, and compatibility with MATLAB and Simulink, which eases control system design.

In addition, PLECS utilises thermal models supplied by component manufacturers such as Wolfspeed (Cree) and Infineon. These provide accurate power loss simulation results based on empirical data contained within lookup tables. By simulating with thermal models and using realistic heatsink and temperature values, the simulation results accurately predict actual component performance in terms of power loss, and temperature.

The initial simulations of the bridgeless isolated converter will be completed without active PFC, using only an output voltage control system. This assures design verification of the converter. An active PFC control system will then be designed in Simulink and tested through simulation to verify active PFC control for the bridgeless isolated converter. These simulation results will be compared to IEC standard requirements.

4.2 Converter Simulation

The full power electronic circuit to be simulated is given in Figure 23. Two back to back Zener diodes are used to simulate a TVS diode clamping circuit, which is used to limit the overvoltage caused by the resonant inductor L_r. Series equivalent resistances are included for key components.

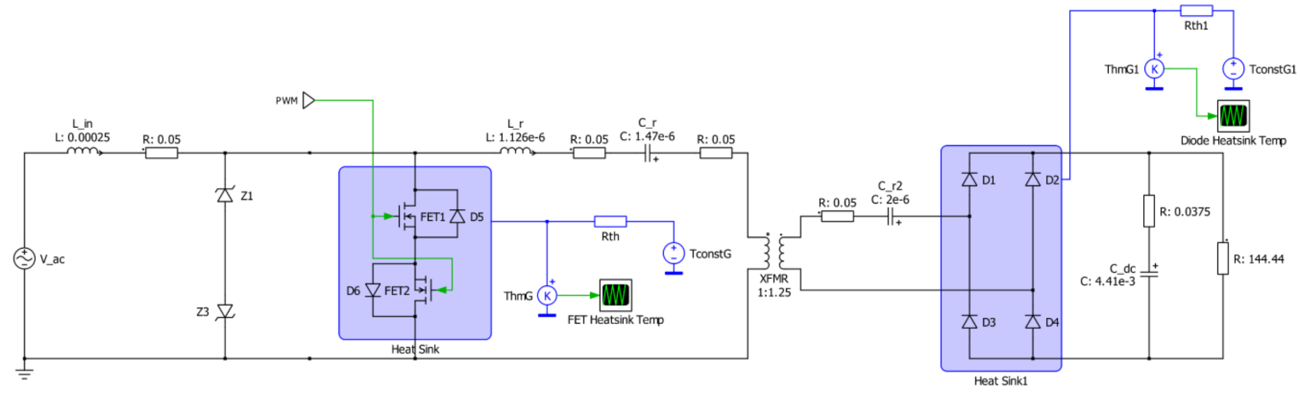

Figure 23: PLECS circuit with thermal models

4.2.1 Thermal Models

One key benefit of using the PLECS simulation system is its thermal models of semiconductor components. PLECS undertakes simulations using ideal semiconductor components, which greatly reduces simulation time (as semiconductor states are taken as either on, or off). Semiconductor voltage and current and temperature parameters are recorded before and after each switch state, and a lookup table containing device parameter data from the manufacturer is used to estimate switching losses. The conduction losses are calculated using the semiconductor current, junction temperature, and corresponding on-resistance for these parameters. This approach gives fast, accurate results.

By combining the use of these thermal models with PLECS's heatsink feature, shown as the blue areas Figure 23, realistic component temperatures can be simulated using real-world heatsink parameters and ambient temperatures. This aids in heatsink design, component selection, and PCB design.

4.2.2 *Component Selection*

Utilizing the features of PLECS, switching component selection can be undertaken, based on simulation results that use semiconductor thermal models available from manufacturers. As the converter operates with both a high-power level and high switching frequency, Silicon Carbide (SiC) MOSFETs and diodes are suitable solutions for the converter, due to their low on resistances, fast switching, and high voltage ratings.

A popular manufacturer of SiC semiconductors is Wolfspeed (Cree Semiconductor). Since Wolfspeed offers PLECS thermal models, this is a convenient starting point for the component selection. Therefore, the simulations will be undertaken using various SiC MOSFETs to compare the power losses and select the most suitable option.

Table 4: PLECS thermal model results for 230V 2kW simulation

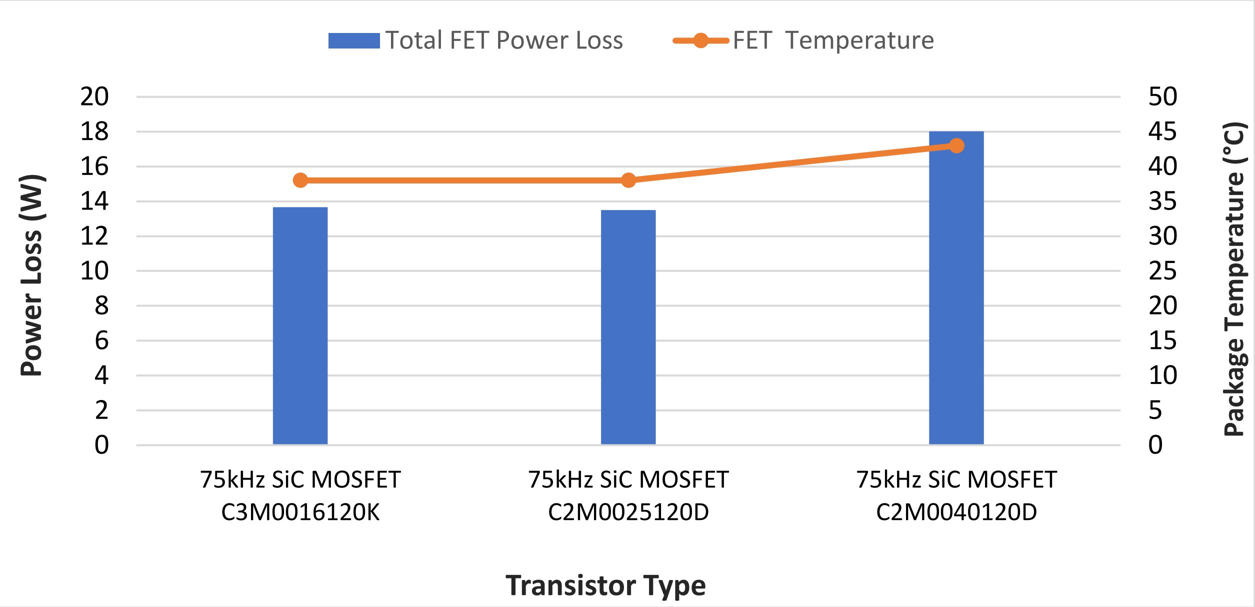

The data gathered from the thermal model simulation is consolidated into Table 4, and the total losses and heatsink temperatures for three different SiC MOSFETs are compared. The C2M0025120D is the MOSFET chosen for the prototype and the remaining simulations, as it is the most efficient. The same process is then followed for the SiC diodes used in the output rectifier, and appropriate diodes were selected. This also allowed the correct sizing for the heatsinks for the semiconductors.

4.2.3 Converter Gain

One of the most important things to verify in the simulation is the conversion ratio defined by (3.7) and derived in Section 3.2.1. Substituting for the chosen winding ratio results in the ideal converter gain. The verification of this gain is critical as this has been used as a basis for the design of all converter components.

The voltage gain is measured using PLECS and data recorded over a wide range of duty cycles, using a constant input voltage while measuring the output voltage. The gain is then calculated for each duty cycle and graphed against the ideal converter gain in Figure 24

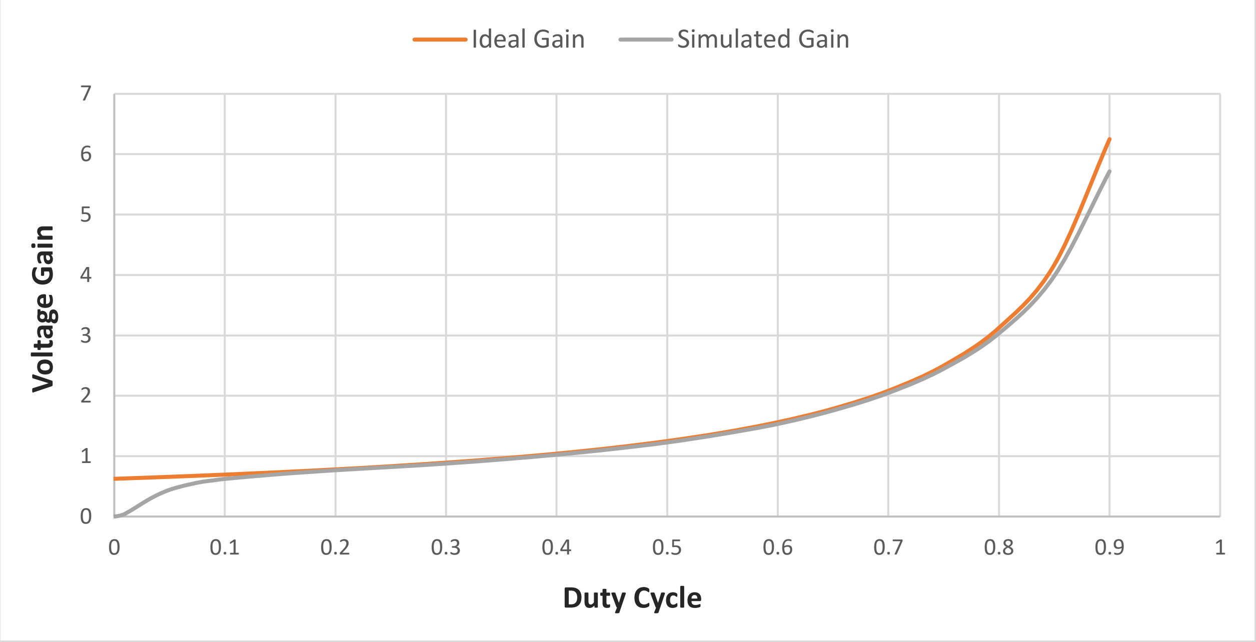

Figure 24: Simulated converter gain vs ideal gain

It can be seen in Figure 24 that the simulated converter gain fits the derived ideal converter gain, although the simulated gain drops to zero at low duty cycles. This is caused by the series resonant circuit, which acts as a series bandpass filter. Due to this, the resonant circuit has a very high impedance at low frequencies, thereby limiting current when the duty cycle is low. This is an advantage of the bridgeless isolated converter, as very low gain occurs at low duty cycles, which suits the implementation of a soft start feature. This also allows the converter to be completely turned off using the switch, as at a low duty cycle there is no output voltage.

The gain of the converter also deviates at higher duty cycles, which is to be expected as the ideal gain will tend to infinity as the duty cycle approaches one. A duty cycle of one would create one current loop consisting of only the input inductor and the voltage source, and therefore no output voltage can exist. The converter gain can also be verified by simulating the converter at maximum and minimum input voltages as seen in Figure 25 and Figure 26. It is apparent that the simulated converter can provide a regulated output voltage, regardless of the input voltage. This verifies that the operation shown in Section 3.2.1 is true across the entire input voltage range.

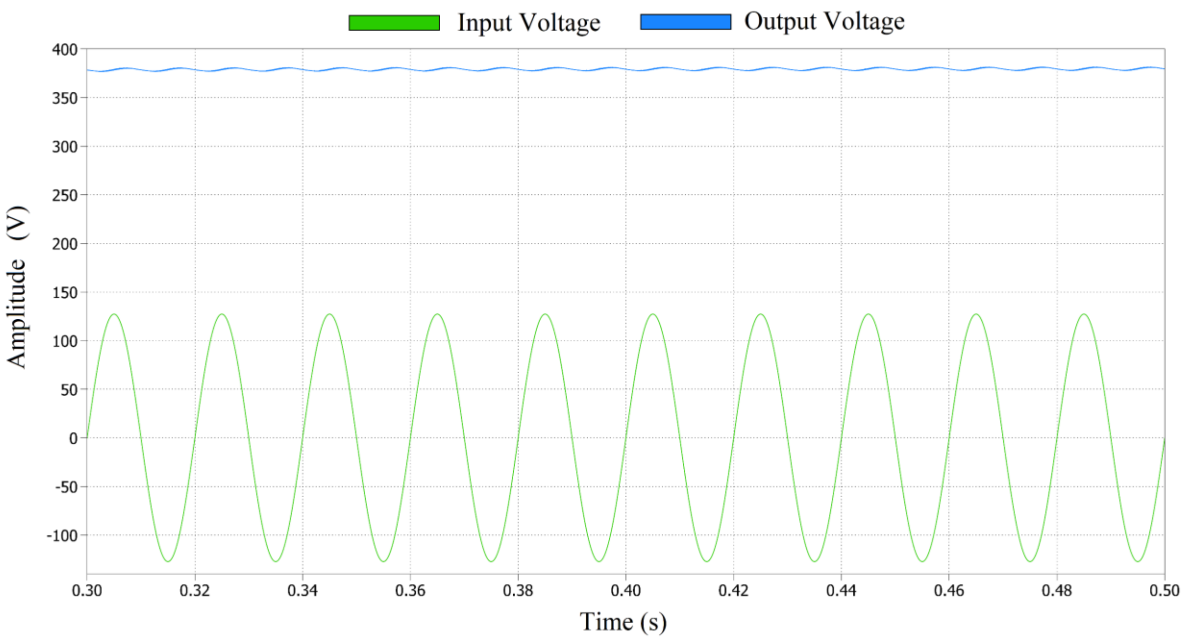

Figure 25: 90 V input, 380 V output, 2 kW

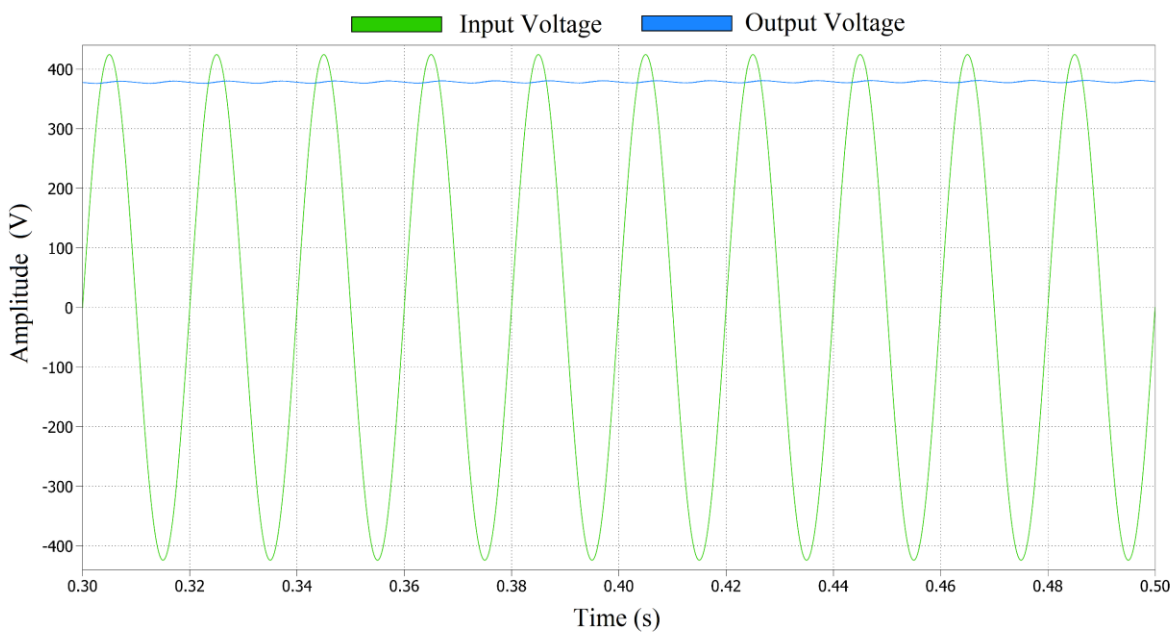

Figure 26: 300 V input, 380 V output, 2 kW

4.3 Voltage Control Simulation

To further verify the theoretical design, the converter is modelled with a voltage control system to regulate the output voltage, and without active PFC. This allows for verification of the component design without the added complication of active PFC control system and decreases simulation time. This also allows for results to be gathered without active PFC operation for comparison to results with active PFC implemented.

The voltage control system is a simple PI feedback control system as shown in Figure 27.

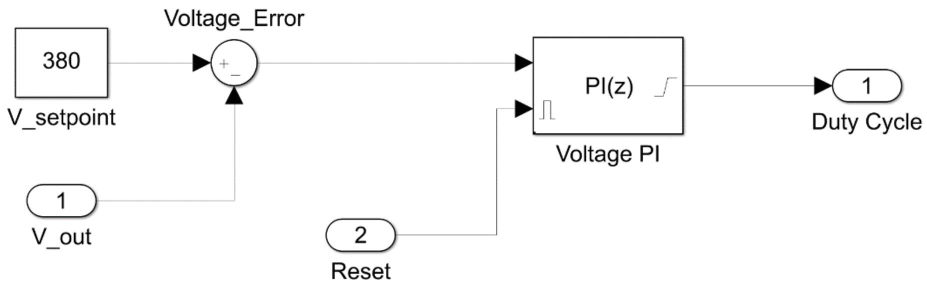

Figure 27: Output voltage controller (Simulink)

This voltage controller calculates the error between the voltage setpoint (V_setpoint) and the actual output voltage (V_out), measured at the load. This voltage error is then fed into a Proportional Integral (PI) controller, which adjusts the output to bring the actual voltage closer to the setpoint. The output of the PI controller is the duty cycle, which is then fed into a modulator to produce the switching waveform at 75 kHz. The integral action of the PI controller accumulates over time, and therefore any steady-state error in the output voltage is removed. This provides an accurate, smooth, regulated output voltage.

4.3.1 Harmonic Content

Using a 230 V input and 2 kW output power for the simulation, the displacement power factor can be calculated by measuring the Δt between the peaks of the voltage and current waveform. With the displacement power factor calculated, this can be used together with measured THD to give the true power factor.

$$\text{Displacement PF} = \cos(\phi) \tag{4.1}$$

Measuring a Δt of $387\ \mu s$ from Figure 29, and the fundamental frequency of $50\ Hz$, the displacement power factor is calculated using (4.1) resulting in a displacement power factor of 0.993. Although this is a good power factor, it does not include the effects of harmonic distortion.

THD can be measured directly in PLECS, and a Fourier analysis can be used to visually display the harmonic content. The THD is measured to be 97.22%, meaning that the amount of harmonic content is almost equal to the fundamental content. This clearly shows the need for active PFC when operating at higher power levels, as IEC standards such as 61000-2-2 recommend limiting THD to less than 5%.

With the measured THD, the true power factor can be calculated using (4.2) [34], which emphasises the difference between displacement and true power factor, and therefore the importance of reducing harmonic content.

$$\text{True PF} = \cos(\phi) * \frac{1}{\sqrt{1 + THD^2}} \tag{4.2}$$

Using the displacement power factor of 0.993 calculated using (4.1), and the THD of 97.22 %, (4.2) can be used to calculate a true power factor of 0.712. This is a poor power factor compared to the displacement power factor and emphasises the importance of measuring THD.

The harmonic content of the input current can be seen visually in Figure 28, which is the output of the Fourier analysis in PLECS. Each harmonic is shown as a fraction relative to the fundamental frequency of 50 Hz. This shows that without active PFC, there is a large amount of harmonic distortion, mostly in the third, fifth, and seventh harmonics.

This is then compared with the IEC standard 61000-3-12 which outlines the harmonic current limits for equipment connected to low voltage public grids [35]. This standard is chosen, as the rated input current of the converter is $22\ A$ due to the low input voltage, and the other closest applicable standard, 61000-3-2, does not apply to grid voltages below $220\ V$. However, these standards have similar harmonic limits and for the sake of initial analysis, 61000-3-12 appears to be the most applicable. The specific harmonic limits for each harmonic are shown in Appendix 1 and it can easily be seen in Figure 28 that without active PFC, the converter does not meet the 61000-3-12 standard.

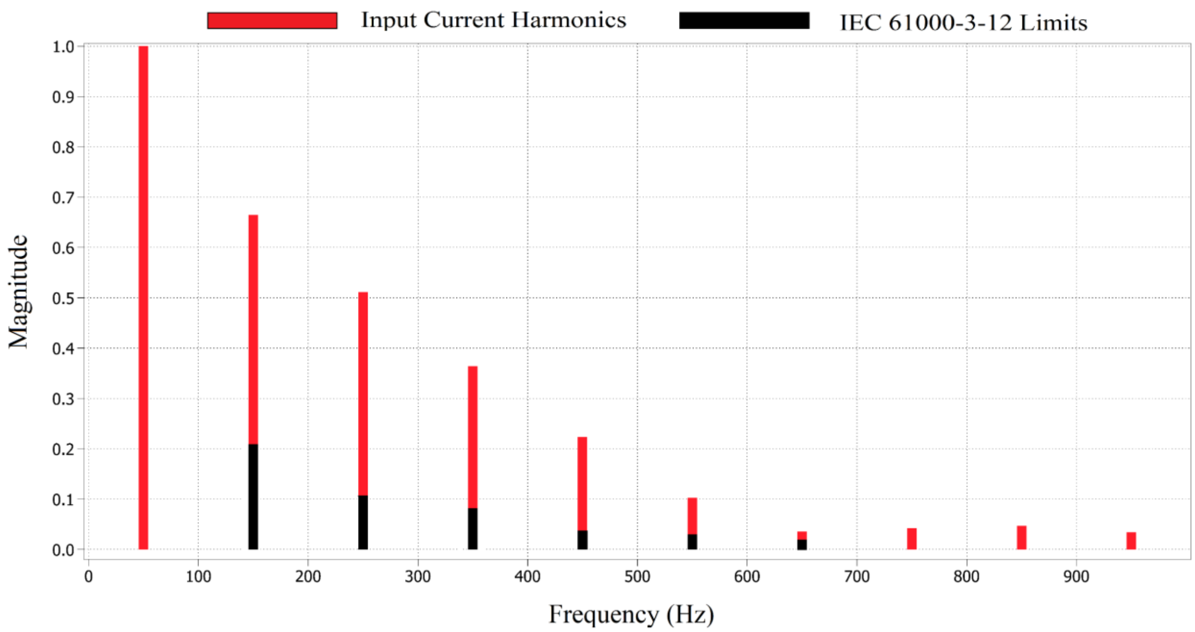

Figure 28: Input current harmonics without active PFC control system

The current distortion can also be seen in

Figure 29, as the input current is showing the distortion typical for a rectifier with a capacitor input filter. It is also seen that the peak currents are much higher than they would be if the input current were purely sinusoidal. This increases conduction losses and therefore decreases converter efficiency, further showing the need for active PFC.

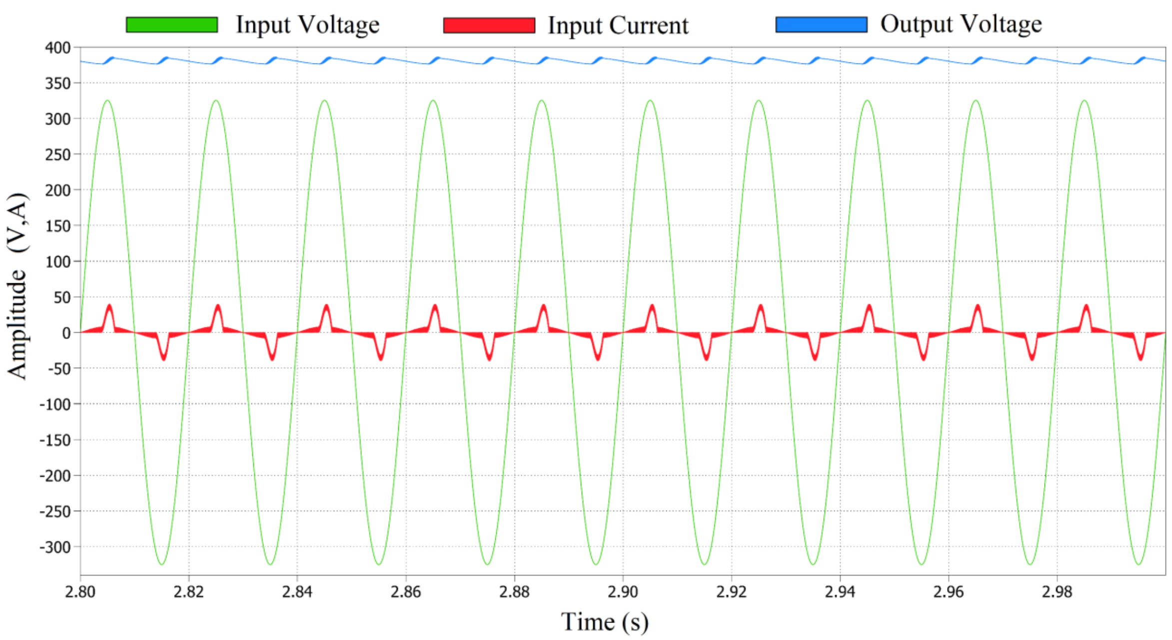

Figure 29: Operation for 230 V input, 380 V 2 kW output without active PFC

4.4 Active PFC Simulation

The results in Section 4.3 highlight the need for active PFC. In this section, an active PFC controller is presented. The controller comprises two control loops, for voltage and current respectively, shown in Figure 30. The outer control loop is a slow sampling voltage PI controller, which compares the output voltage to the specified setpoint voltage to calculate the error for the voltage PI controller. This voltage controller outputs a reference of the magnitude of the current required to reduce the voltage error to zero. This is then multiplied with a reference current waveform, to provide a complete reference current of correct shape, phase, and magnitude.

The second control loop controls the input current and shapes it to the shape, phase, and magnitude of the reference current waveform. This control loop operates at a much higher sampling frequency than the outer voltage loop, as this needs to adjust the duty cycle constantly across the input period to accurately shape the input current.

The setpoint for the error calculation is derived from the input voltage, by sampling the input voltage to provide a sinusoidal waveform and normalizing it to a magnitude of 1. By multiplying this waveform by the current magnitude provided by the voltage controller, a reference current is provided that is the same shape as the input voltage, the magnitude of which changes to regulate the output voltage. This reference current is then compared against the sampled input current, and the error is fed into the current PI controller. The output of this controller is the duty cycle, which is fed into a 75 kHz modulator. This control system can then regulate the output voltage while shaping the input current simultaneously.

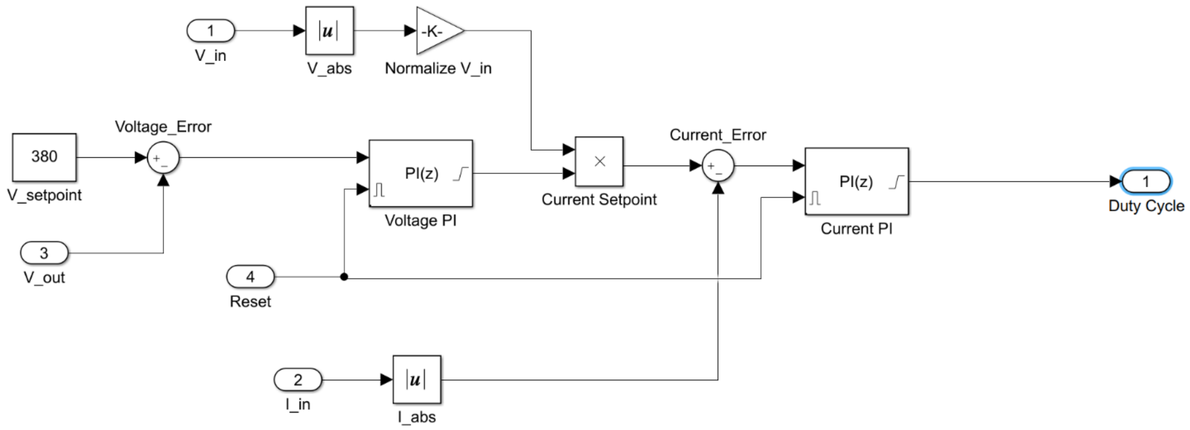

Figure 30: Active PFC and output voltage controller (Simulink)

4.4.1 Harmonic Content

Integration of the active PFC controller with the isolated bridgeless converter allows simulations to be run for comparison with results from Section 4.3.

Measuring a difference of $\Delta t = 6.29\ \mu s$ between the voltage and current waveforms shown in Figure 32 allows the calculation of the displacement power factor using (4.1). This results in a displacement power factor of 0.999.

Measuring the THD using the same method as discussed in Section 4.3 provides a THD of 11.29%. Using the THD of 11.29% and the displacement power factor of 0.999 as calculated from Figure 32, the true power factor can then be calculated. Using (4.2), the true power factor is calculated to be 0.994.

This is a significant improvement than the results shown in Section 4.3, which can be visualised in Figure 31, where it is compared with the IEC 61000-3-12 harmonic limits. This shows that with the active PFC system, the bridgeless isolated converter is capable of meeting the 61000-3-12 standard, although it is very close to the limits for the third and fifth harmonics. This could easily be improved further through the placement of a suitable input filter.

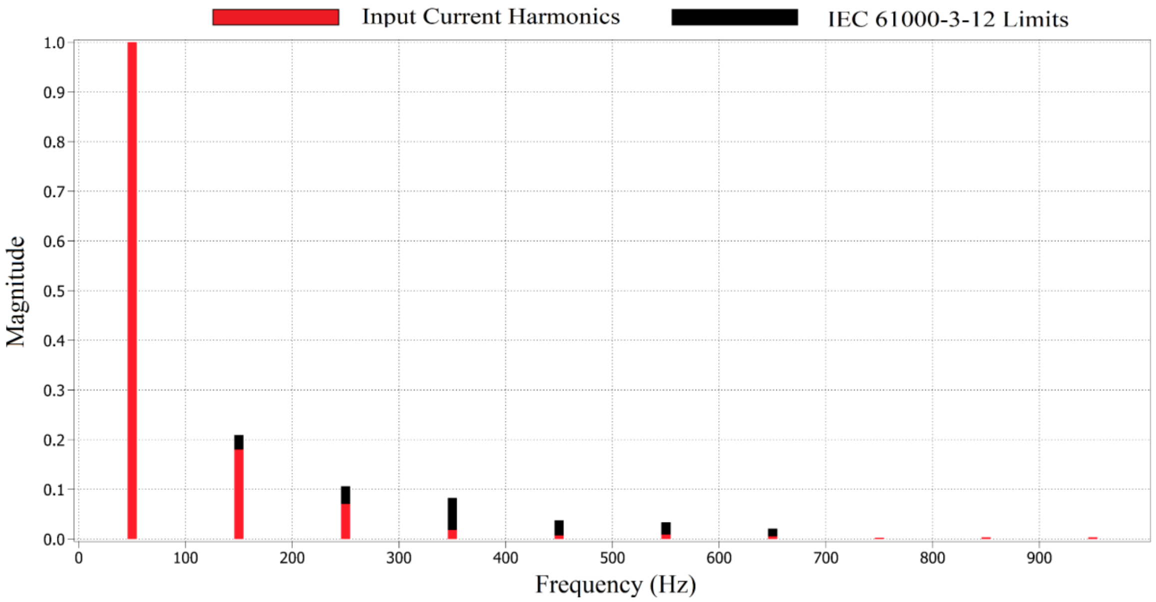

Figure 31: Input current harmonics with active PFC control system

The improvement in the input current shaping is visible in Figure 32, as the input current follows a sinusoidal shape with a small amount of distortion around the zero crossings of the input voltage. The peak currents are also reduced greatly when compared to the input current without active PFC, for the same power level.

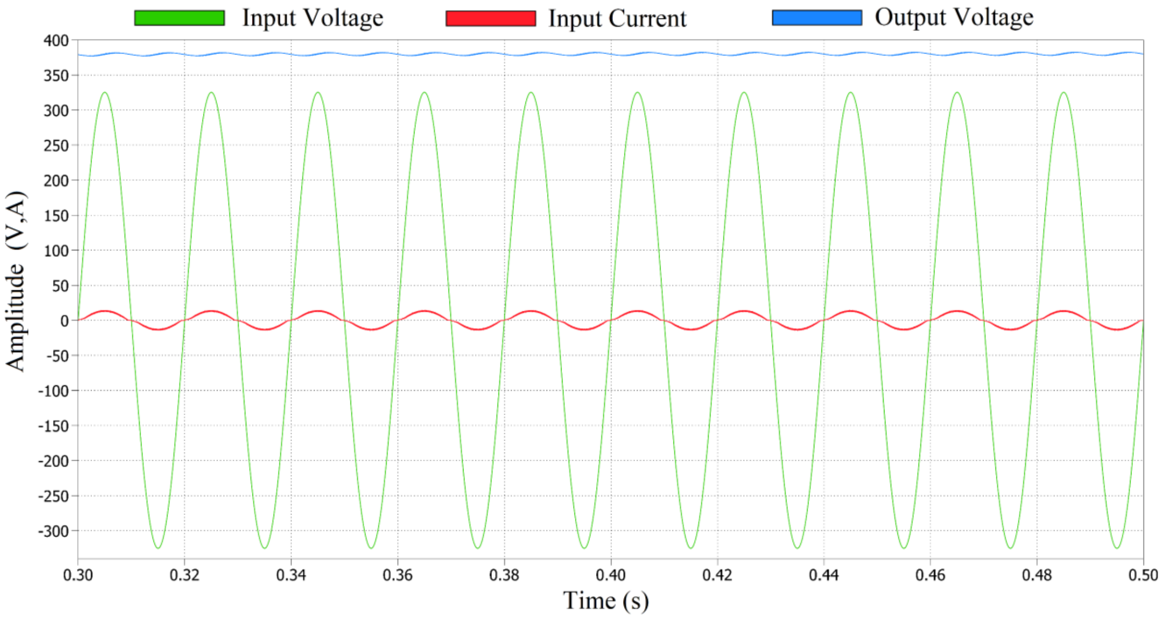

Figure 32: Input voltage, input current and output voltage for 230 V input, 380 V 2 kW output with active PFC.

4.5 Resonant Operation

The resonant operation is another important part of the proposed design procedure that can be verified through simulation. Verification is undertaken using a 230 V input, a 380 V, 2 kW output, and an active PFC control system, as the theoretical design assumes a sinusoidal input current.

The first step of the design procedure is to calculate the resonant frequency based on the minimum duty cycle. The minimum duty cycle range is decided by the required conversion ratio and maximum acceptable resonant frequency. The voltage gain has been verified in Section 4.2.3, and therefore the minimum duty cycle design in Section 3.2.4 is valid. Therefore, the design of the resonant frequency is also considered valid. To confirm that the chosen resonant components do indeed provided resonance at the designed frequency, the period of the resonant current can be measured.

The resonant current can be seen in Figure 33 over multiple switching cycles. It can be seen that during t_{off} the resonant current is positive and equal to the magnitude of the input current, and during t_{on} the resonant current is negative and shows the half-sinusoidal shape expected of the resonant current. From this, the resonant frequency can be confirmed as the resonant current will only exist for half a cycle of the resonant period. The time of half a cycle is calculated to be $3.33 * 10^{-6}\ s$ using the designed resonant frequency of $150\ kHz$. The time period of the resonant current is measured to be $3.341 * 10^{-6}\ s$, which equates to a resonant frequency of $149.65\ kHz$.

This is a small margin of error compared to the designed resonant frequency, although this could be caused by measurement error as the PLECS solver calculates in discrete steps, and therefore cursor measurements will jump to the nearest discrete step. Notwithstanding a small error in the resonant frequency, the simulation results verify the resonant circuit design approach in Section 3.2.4. The results also show the magnetising inductance and other components do not have a significant effect on the resonant frequency during t_{on}.

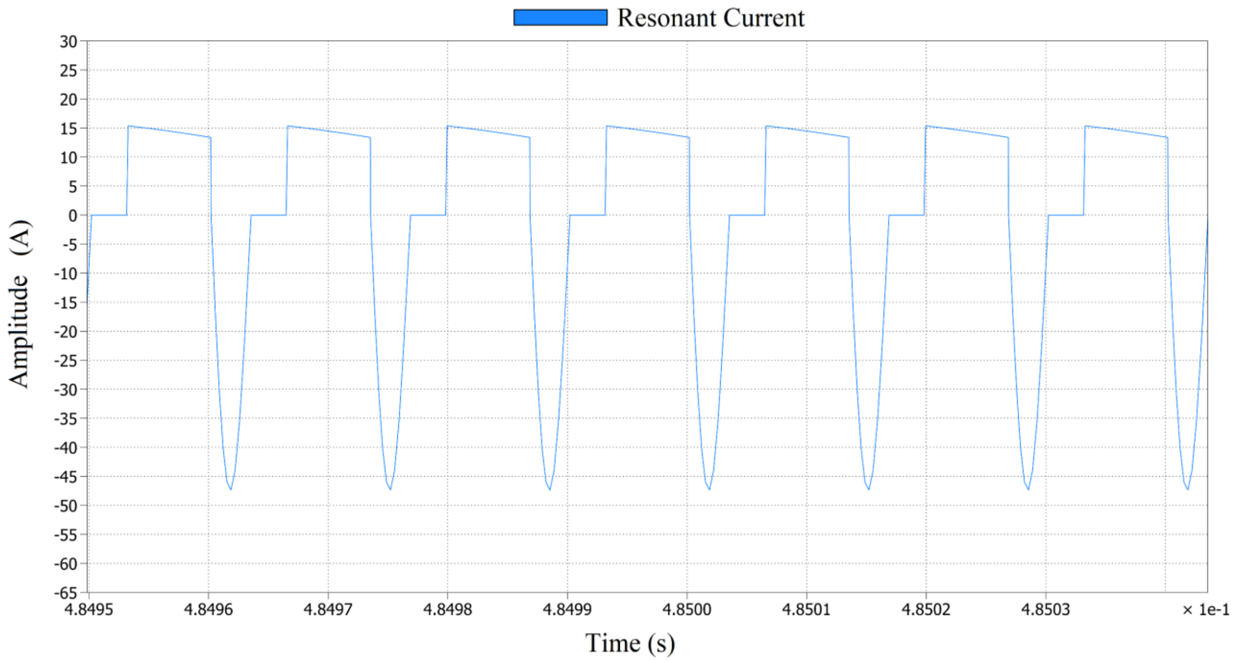

Figure 33: Resonant current at switching frequency

The second step of the design procedure is the design of the minimum resonant capacitance. Equation (3.5) shows that the equivalent resonant capacitor voltage must charge up to $\frac{V_o}{n}$ during positive input voltage and $-\frac{V_o}{n}$ during negative input voltages.

This can be shown in simulation by summing the two capacitor voltages while accounting for the winding ratio and displaying both the summed capacitor voltage and the scaled output voltage. This is also shown mathematically in (3.5).

From Figure 34 it is apparent that V_{C_r}, the sum of the resonant capacitor voltages $V_{C_{r1}}$ and $\frac{V_{C_{r2}}}{n}$, charges to an average voltage of $\frac{V_o}{n}$ and $-\frac{V_o}{n}$ for positive and negative input voltages respectively. The ripple voltage ΔV_{C_r} is centred on this average voltage, and it is clear that the larger the ripple voltage is, the higher the peak of V_{C_r} will be.

As per (3.4), $V_{C_r} + \frac{V_o}{n}$ is imposed across S_1 during t_{on}, and can be seen in Figure 35. This shows that an increase in capacitor ripple voltage directly increases the peak switch voltage.

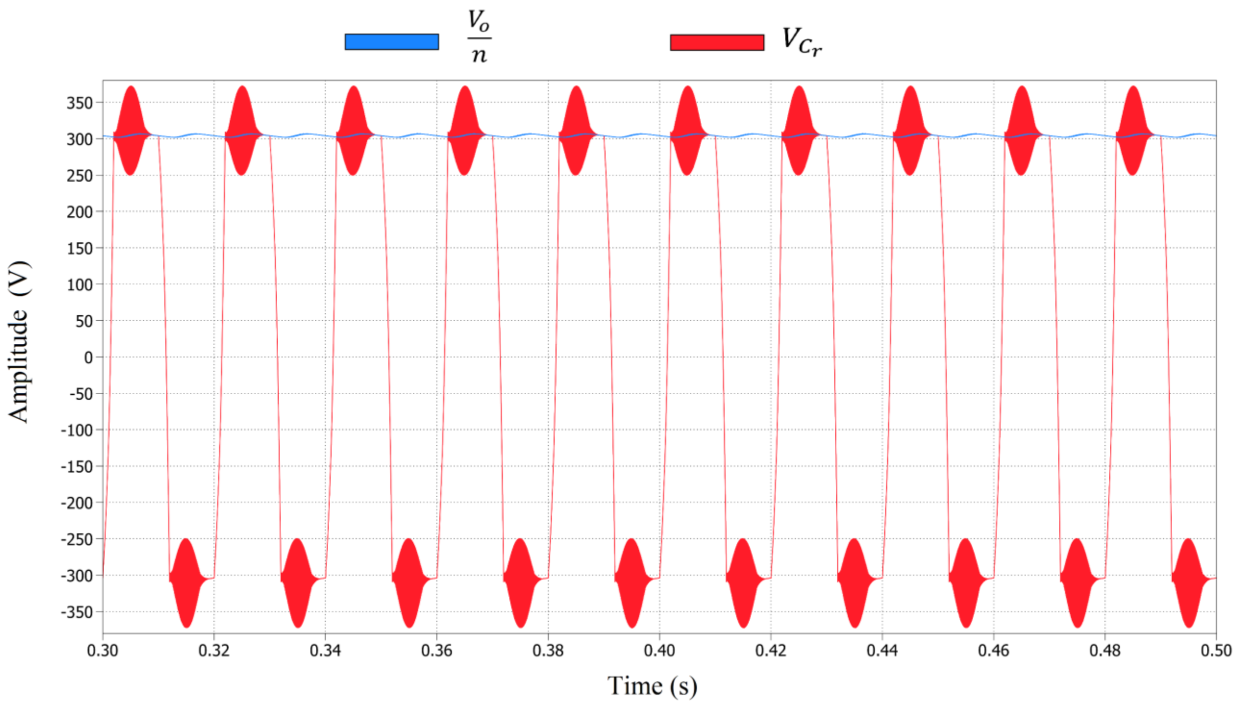

Figure 34: Equivalent resonant capacitor voltage $\left(\boldsymbol{V_{C_r}}\right)$ and equivalent output voltage $\left(\frac{\boldsymbol{V_o}}{\boldsymbol{n}}\right)$

The ripple voltage on the capacitor can confirm the linear approximation that is made in the resonant design procedure, for which the charge balance rule is used to approximate the ripple voltage and, therefore, the switch voltage.

Using (3.14) the ripple can be calculated based on the total equivalent resonant capacitance, which can then be compared to Figure 35 to identify any margin of error in the approximation. Since the simulation has an input voltage of $230\,V$, the peak capacitor current during t_{off} must be calculated.

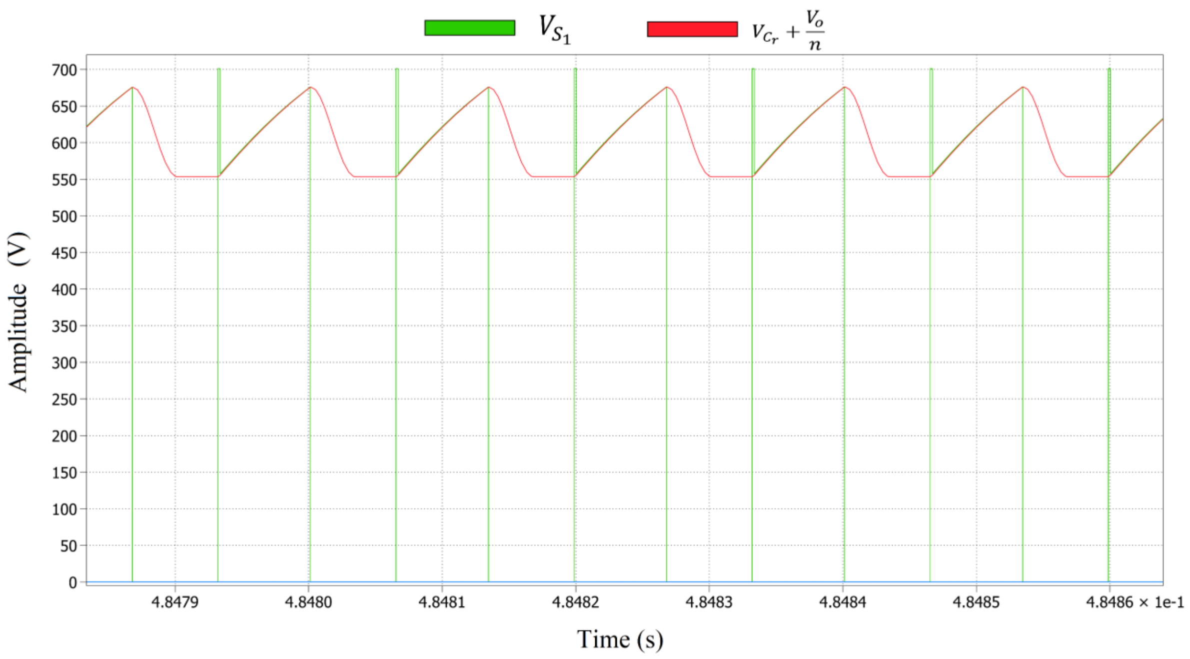

Figure 35: Switch voltage ($\boldsymbol{V_{S_1}}$) and $\boldsymbol{V_{C_r} + \frac{V_o}{n}}$

As shown in Section 3.2.4, the capacitor current during t_{off} is equivalent to the input inductor current, which can simply be calculated using the ripple current ΔI_{L_i} of $7.77\ A$, and the input current of $12.3\ A$ when using a 230 V input voltage. This provides a peak current $I_{C_r\,max\,(t_{off})}$ of $16.17\ A$.

The duty cycle required for a 230 V input voltage is calculated using (3.7) and results in a duty cycle D of 0.465. Substituting D and $I_{C_r\,max\,(t_{off})}$ into (3.7) results in a maximum capacitor ripple voltage $\Delta V_{C_r\,max}$ of $115.3\ V$. This can then be used to calculate the peak switch voltage, using (3.13). This results in a maximum switch voltage of $665.65\ V$.

The simulated ripple voltage is measured to be $117.12\ V$, with a maximum switch voltage of $676.7\ V$, not including the clamped inductive spike. The small error in the approximation exists as the charging of a capacitor is not a linear relationship, but the approximation used is linear. Since the error is only 1.5%, the linear approximation is an accurate approximation for the design procedure, as long as a margin for the switch voltage rating is maintained to account for this error.

The overvoltage of the switch due to the resonant inductor can also be seen at the start of the switching waveform, where it is clamped to $700\ V$ due to the TVS clamp in the simulation. The duration of this overvoltage is quite a short time and, therefore, can be successfully clamped using TVS diodes, although this results in $60\ W$ of losses at the maximum input current of $22\ A_{rms}$. This is a 3% loss of efficiency which is quite significant, and therefore it is preferred to use a lower loss snubbing technique. However, this is satisfactory for the initial simulation and verification purposes.

To show the effects of non-optimal resonant components, the resonant capacitors are decreased by a factor of four, and the resonant inductor increased by a factor of four. This pushes the components outside of the optimal range outlined in the design procedure, thereby allowing for comparison with optimal range results.

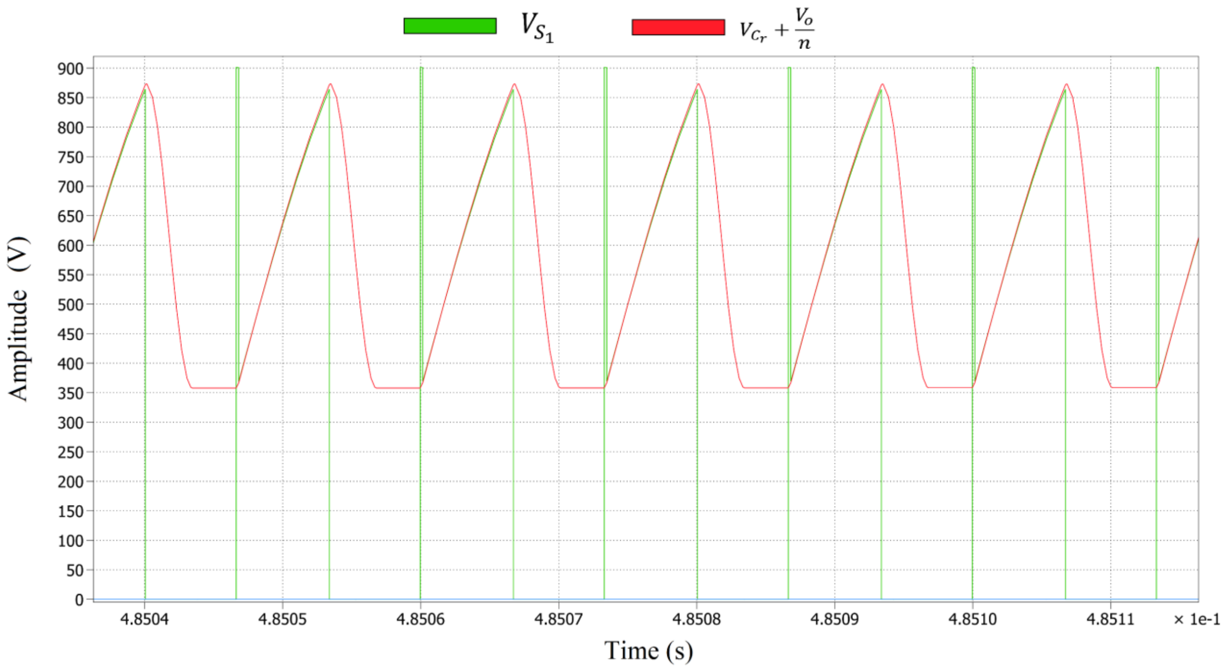

Figure 36: Sub-optimal resonant components

Figure 36 shows the switch voltage waveforms with the sub-optimal resonant components. While the average switch voltage is still $\frac{2V_o}{n}$, the peak switch voltage is much higher due to the higher ripple voltage on C_r and, therefore, the rating of the switch must be increased. This also forces the clamping voltage of the TVS clamp to increase to 900 V so that it does not impede the normal circuit operation.

Increasing this clamp voltage does slightly reduce the losses in the TVS clamp to 50 W, although it forces the use of 1200 V MOSFETs, which can have worse performance than their lower voltage counterparts. This shows that the design of the resonant circuit is crucial, as it can cause a large variation in required component ratings, without any change in input or output specifications.

4.6 Conclusion

The final design of the converter is shown in Figure 22 and the design procedure for the resonant circuit has been verified, along with the full operation and control of the converter through simulations in PLECS and Simulink. The design procedure is shown to have a small margin of error due to linear approximations, although these are considered acceptable and do not have a significant effect on the design of the circuit.

It is shown that the bridgeless isolated converter can operate with active PFC and that the harmonic content is greatly reduced. The overvoltage of S_1 is clamped using a TVS diode configuration, however, this results in a significant reduction in efficiency. Accordingly, and for prototype development, lower loss snubbers will be employed. With the theoretical design verified through simulation, the prototype can be designed, assembled, and tested for experimental verification.

Chapter 5

Prototype and Testing

5.1 Introduction

To experimentally verify the simulation results in Chapter 4, the test results of a developed prototype are given in this chapter. The hardware design aspects such as the switching devices, magnetics components, PCB design, and resonant circuit are discussed, and revisions to the component designs are made to accommodate design tolerances. Following the hardware design description, control implementation is briefly discussed, before test results are presented. The test results are given for the converter operating as an AC/DC converter and to the specified power and voltage levels, but without active PFC. This was not implemented, due to time constraints.

5.2 Prototype design

The prototype design needs to allow for a programmable control system so that voltage control and active PFC can be implemented without any need for hardware changes. To allow for this, isolated voltage and current sensors are to be used to provide feedback for the control system. The prototype also allows for test points for easy measurement reading and confirmation of the circuit operation. Larger and key components of the converter are described in Section 5.2.1

5.2.1 Component Design

Semiconductor Selection

In Chapter 4, Wolfspeed C2M0025120D SiC MOSFETs were selected for use, which are rated to 1200 V and have an on-resistance of 25 $m\Omega$. 1200 V rated MOSFETs were chosen so that a large margin of error could be maintained for all testing of the active snubber and resonant configurations, although the design procedure has shown how to correctly design the resonant circuit for MOSFETs of a desired voltage rating.

With this selection of SiC MOSFETs, extra care is required when designing the gate drive circuitry, as SiC MOSFETs have different drive requirements compared to standard Si MOSFETs. This includes a need for negative gate voltages to turn off the MOSFET. One convenient SiC gate drive solution is the Texas Instruments UCC53x0 series. These drivers run from a +20 V / -5 V isolated supply and, therefore, can directly drive MOSFETs without the need for a bootstrap circuit or other complicated drive configurations.

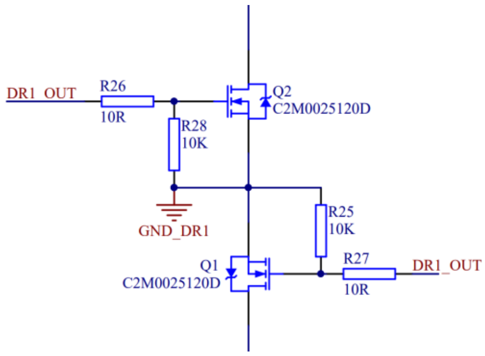

Figure 37: Common source MOSFET configuration

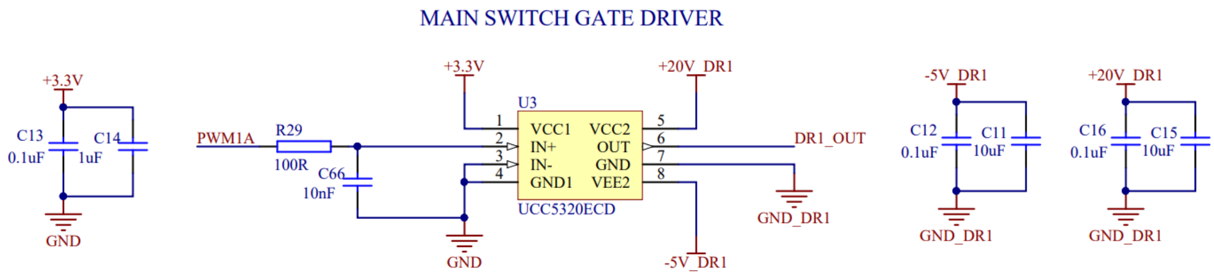

Figure 38: Isolated gate driver configuration for SiC MOSFETs

For the output diodes, the Wolfspeed CVFD20065A SiC Schottky diodes were chosen for their low forward voltage and negligible reverse recovery time, thereby eliminating switching losses.

The output capacitance is achieved using four parallel 1 mF 450 V electrolytic capacitors, giving a total capacitance of 4 mF.

Magnetic Components

Although designed to specification, small measured variances in the magnetic components existed. This included the input inductor with designed and measured inductances of $260\ \mu H$and $256\ \mu H$, respectively, and the transformer. The transformer has a 1:1.25 winding ratio, as specified by design, but a leakage inductance of 1.5 μH, which varies from the specification of 1.12 μH. Due to this, the required resonant capacitance to achieve resonance at 150 kHz was recalculated While this differs from the initial design, it is still within the optimal range for the resonant circuit shown in Section 3.2.4 and, therefore, is acceptable for the prototype.

To calculate the new required equivalent resonant capacitance C_r, (3.11) is rearranged. Substituting the measured leakage inductance and the resonant frequency of 150 kHz results in a new C_r of $750.5\ nF$. The individual capacitor values comprising C_r are calculated using (3.10). With C_{r2} as $2\ \mu F$, C_{r1} is calculated to be $0.988\ \mu F$, which is rounded to $1\ \mu F$.

The converter design with component values adjusted for manufacturing tolerances is shown in Figure 39 and is implemented for the prototype.

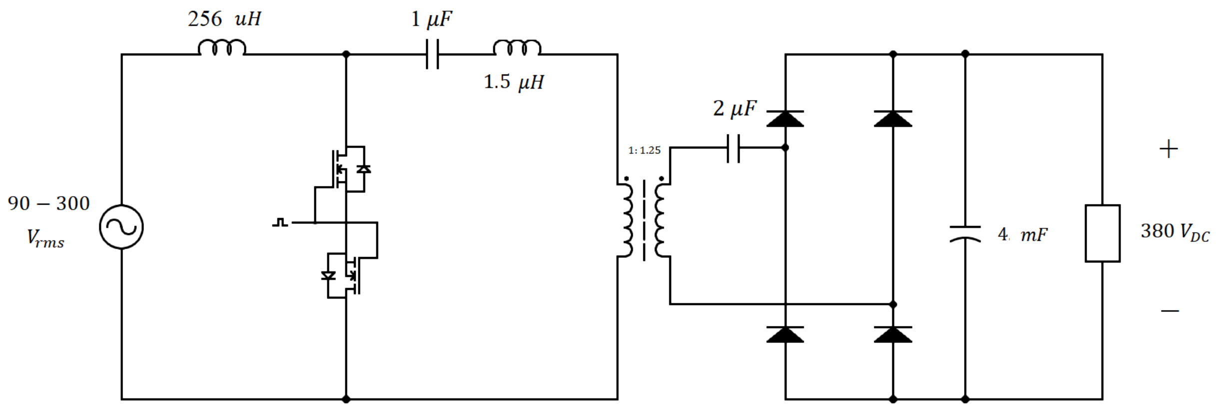

Figure 39: As-built converter design

Control system implementation

To implement the control system a Texas Instruments C2000 LAUNCHXL-F28379D evaluation board is chosen, as this can be directly connected to Simulink. This allows the existing control systems given in Chapter 4 to be programmed directly to the microcontroller. The LAUNCHXL-F28379D evaluation board can also run as a real-time system connected to Simulink so that parameters can be changed, and data viewed in real-time as it interfaces with the converter. This allows for easy prototype tuning and monitoring.

Figure 40: Texas Instruments C2000 LAUNCHXL-F28379D evaluation board

Voltage and Current Sensing

Key features incorporated into the prototype include voltage and current sensors necessary for the voltage and active PFC control systems. These must be as noise-free as possible to allow for smooth control system operation. Consideration must also be given to the fact that all input voltage and currents are AC and, therefore, cannot be fed directly into the LAUNCHXL-F28379D evaluation board.

Texas instruments offer an ideal solution for AC voltage sensing using the ISO224 isolated amplifier series. These isolated amplifiers can take an AC input voltage of $\pm 12\ V$, and output a $4\ V$ differential signal. The differential output provides high noise immunity and a wider sensing range, as it gives an equivalent resolution of $8\ V$. Further, this output can connect directly to the LAUNCHXL-F28379D evaluation board, as the microcontroller used can support differential inputs to the ADC’s with 16-bit resolution. The same isolated amplifier is also used for the output voltage sensing, as it provides up to $5\ kV$ of isolation. Therefore, there are no issues in sensing the isolated output voltage of the converter.

The input and output voltages are reduced to $\pm 12\ V$ using resistive voltage dividers, and since the amplifier allows negative input voltages, no biasing is required.

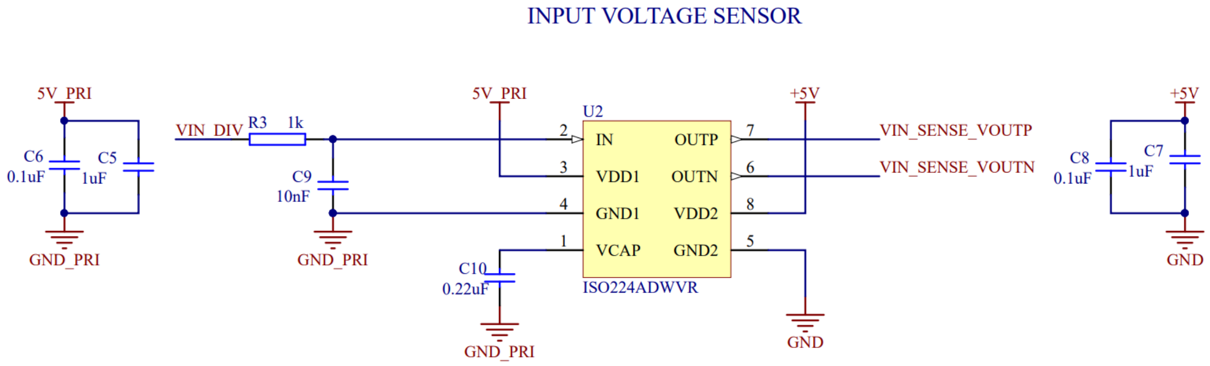

Figure 41: Input voltage sensor (Same as output voltage sensor)

Since differential signals are being used on the voltage sensing, due to their wider resolution and noise immunity, it is desirable to use differential signals for the current sensor also. Therefore, the Allegro Microsystems ACS726 40 A Hall-Effect current sensor is used for measuring the input current. Similar to the voltage sensors, this has a 2 V differential output signal, which can be measured directly by the LAUNCHXL-F28379D.

5.2.2 PCB Design

All PCBs were designed using a 2 Oz copper weight to allow for high currents. The converter is implemented on three different PCBs, as each serves a different purpose. The first is a control PCB, which is used to interface the LAUNCHXL-F28379D evaluation board to the rest of the converter. This essentially connects to the LAUNCHXL-F28379D and breaks out the required ADCs and PWM signals to header pins so that cables can be used to connect to the converter. This board also produces all low voltage supplies required from one main 24 V supply.

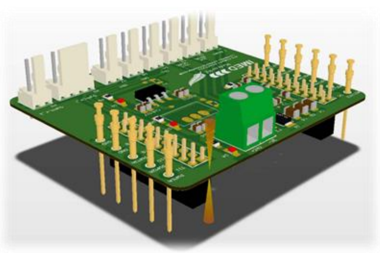

Figure 42: Control PCB for interfacing Launchpad

The remaining two PCBs are the power electronic circuit boards for the converter itself as seen in Figure 43. This is split into two separate boards as the transformer separates the two, and therefore isolation is easily achieved. The primary board contains the input terminals, terminals for the input inductor and resonant components, the main switch, and all input sensors and switch drivers.

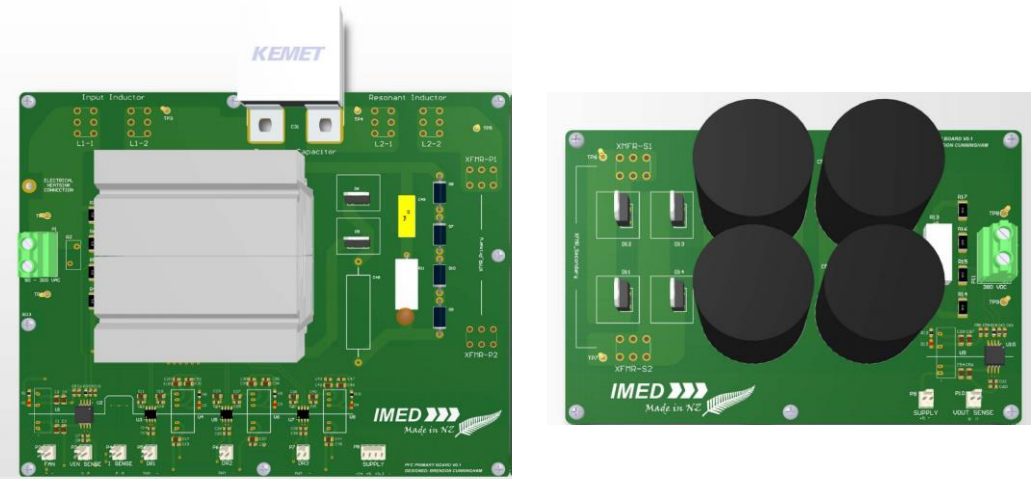

Figure 43: Primary and secondary converter boards

The secondary board circuitry includes the output rectifier, bulk capacitance, output sensors and output terminals. The voltage sensing and control has a dedicated area on each PCB to ensure isolation is kept. To allow the resonant capacitors and the magnetic components to be easily removed and swapped out, screw terminals that allow for lug connection were used for the all magnetic and resonant components.

5.2.3 *Finished Prototype Assembly*

The enclosure designed to house the assembled PCBs and magnetic components is shown in Figure 44. Slots in the sidewalls allow for good airflow, and cable entry on both sides for the supply and load connection. A clear acrylic cover is hinged to the enclosure to guard against high voltage contact.

Figure 44: Final assembled prototype

The total weight of the prototype is 6.35 kgs. The breakdown of the weight of the prototype is shown in Table 5. Since this prototype is only the input AC/DC stage for the entire AC/AC system, it cannot be compared directly to the existing commercial systems shown in Chapter 1. However, since it is discovered that the transformer approximated 56% of one of the AC/AC converters shown in Section 1.1, it could be assumed that the AC/DC stage (including the transformer), would approximate at least 60 % of the total converter weight.

The lightest commercial converter that is shown in Chapter 1 is the Ultra-LP-12 from Atlas Marine Systems, at 10.17 kg/kW. If it is assumed that the input AC/DC stage is 60% of the total weight, then the AC/DC stage can be approximated as 6.102 kg/kW. In comparison, the prototype developed using a high-frequency transformer weighs 3.177 kg/kW, a 48% weight reduction. This shows a potential advantage of the bridgeless isolated converter topology relative to commercial options, although there are significant other components that would be required for the full converter design.

Table 5: Prototype weight breakdown

Component	Weight
Input Inductor	1 kg
Transformer	0.97 kg
Primary Board	0.595 kg
Secondary Board	0.579 kg
Control Board	0.21 kg
Case	3 kg
Total	6.354 kg

5.3 **Results**

5.3.1 Introduction

The specifications of the converter include an input voltage range of 90 V_{rms} to 300 V_{rms}, an output voltage of 380 V_{dc} and an output power rating of 2 kW. To ensure results are can be gathered and to minimize risk, the initial testing is performed using only the output voltage control system, as there is a much smaller margin for error when using the active PFC control system, and more complex tuning is required. Due to time constraints, the active PFC control system was unable to be implemented in the prototype.

The scope of the high voltage AC testing includes measuring efficiency across the entire load range for multiple power levels, thermal measurements of key components, and verification of the design procedure. To verify the active snubber briefly described in Chapter 3, test results are given in Section 5.3.2.

5.3.2 Active Snubber Verification

For the purpose of comparison, the converter is initially operated with a low voltage input, with and without active snubber. This allows for direct comparison, without damaging the circuit high voltage switching devices.

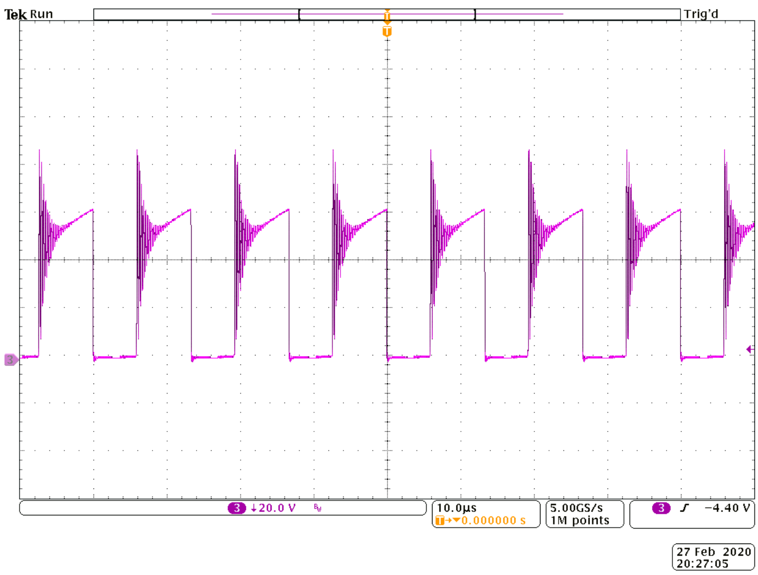

Figure 45: Switch voltage without snubber

Figure 45 shows the switch voltage waveform with no snubbing technique used. It is apparent that the overvoltage caused by the resonant inductor is significant and must be limited, before testing at higher voltages. This highlights the importance of utilizing an active snubber to minimize overvoltage.

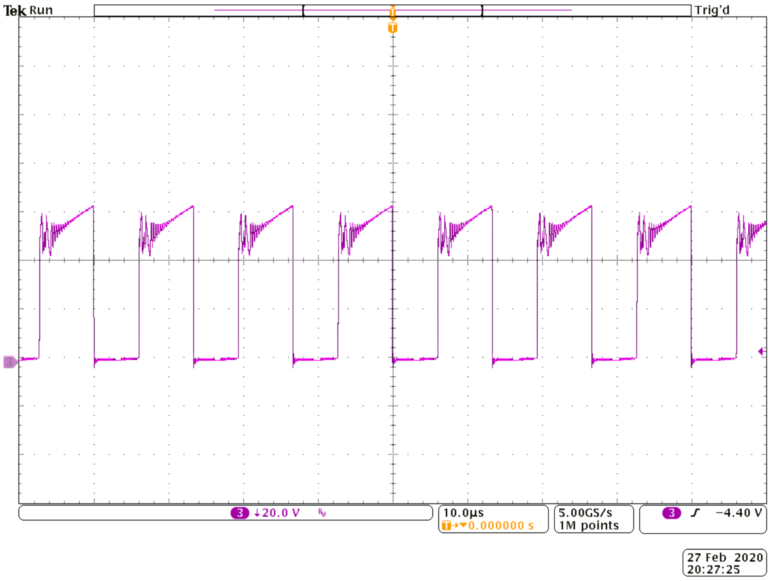

Figure 46: Switch voltage with active snubber

An active voltage snubber as described in-depth in [31] is implemented in the prototype, and the effects it has on the overvoltage is shown in Figure 46. This confirms the operation in [31] and shows that the overvoltage can be limited using an efficient snubbing technique, and therefore is not an efficiency concern. Due to the in-depth analysis in other literature, overvoltage and active snubber operation are not discussed further.

5.3.3 *Test Results*

Testing is conducted over the input voltage range of 90 V_{rms} to 265 V_{rms}, due to limitations in the availability of high voltage AC supplies rated to 300 V_{rms} . The input to the converter is derived from a 20 A_{rms} , 0 – 265 V_{rms} variable AC supply. The load used is a Chroma DC electronic load as shown operating in Figure 47, which can be programmed for a wide range of loads and can dissipate up to 5.2 kW at 600 V_{dc}. Simulink was used to interface to the LAUNCHXL-F28379D, to allow monitoring of input and output voltages and currents as shown in Figure 48.

Figure 47: DC load at full rated output power

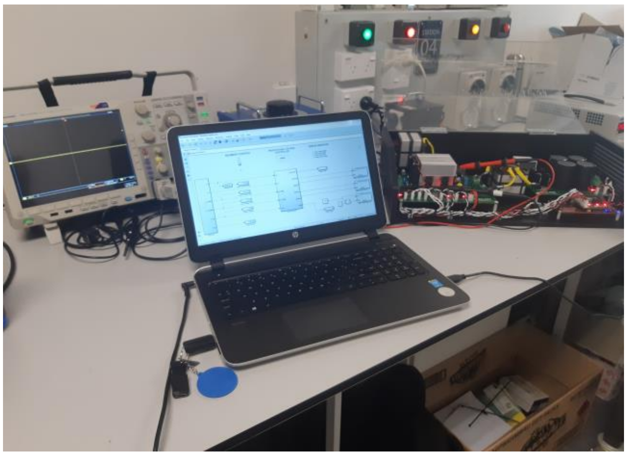

Figure 48: Testing area with interface to LAUNCHXL-F28379D

The wide input voltage range is confirmed at both 90 V_{rms} and 265 V_{rms} AC input voltages and waveforms of each are shown in Figure 49 and Figure 50. It can be seen from these figures that both the low and high ends of the input voltage range can both produce a 380 V_{dc} output. The scope figures show a small margin of error in the output voltage regulation, which is due to the control system not being optimally tuned and therefore the output voltage can drift a small amount, before integral action correction.

Although the resolution of the oscilloscope images is low, the output voltage ripple for both tests can be seen clearly at a frequency of 100 Hz, as expected.

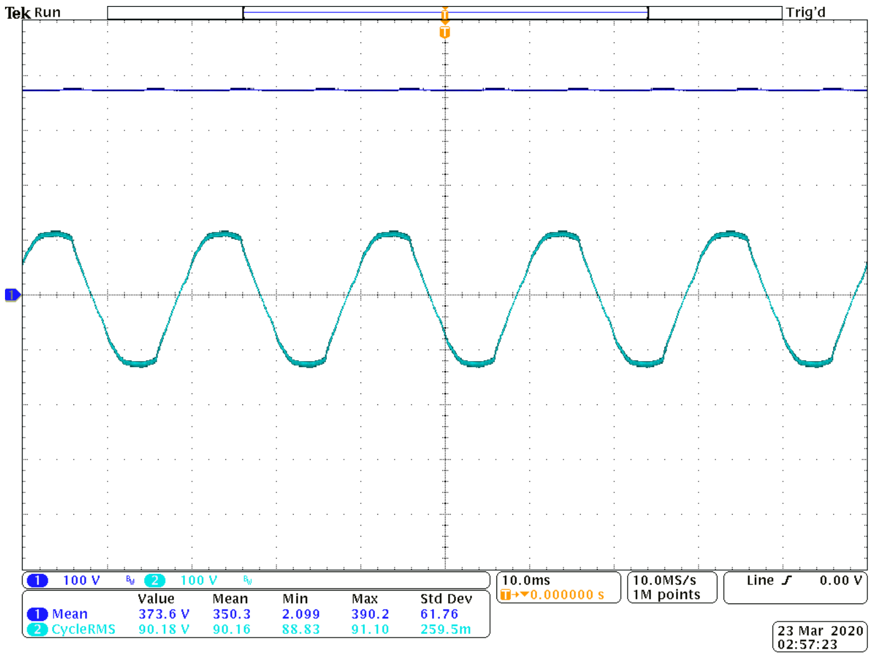

Figure 49: 90 V AC input, 380 V DC output

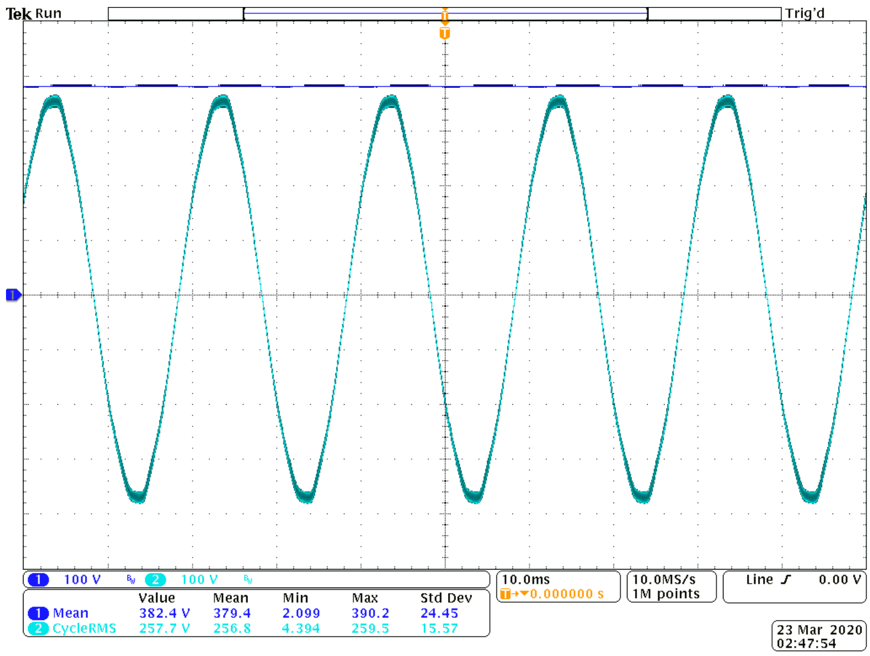

Figure 50: 265 V AC input, 380 V DC output

Figure 51 shows the output voltage waveform with AC coupling applied the oscilloscope. This allows for closer examination of the ripple voltage. As shown in Section 3.2.5, the output capacitors were designed to have a ripple voltage of 1%, which is a 3.8 V_{pk-pk} ripple on the output voltage waveform. This is confirmed in Figure 51 which shows an approximate 3.75 V_{pk-pk} ripple on the output voltage waveform.

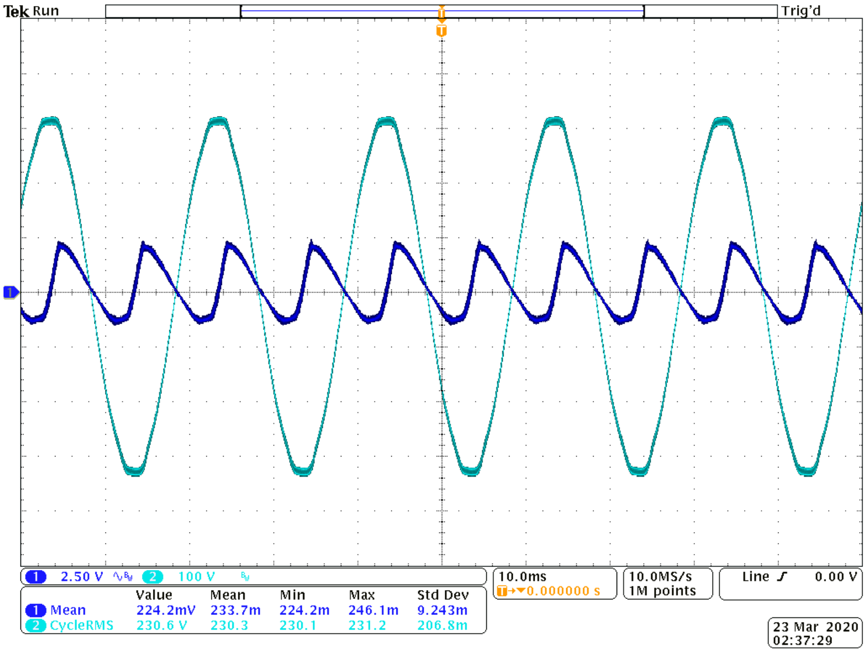

Figure 51: AC coupling of the output voltage waveform

The high voltage AC testing is conducted at various power levels to gather a wide range of data for analysis. Since active PFC has not been implemented in the experimental prototype, the output power is limited to 1 kW when testing with an input voltage of 90 V_{rms}. This is due to the peak currents being much higher without active PFC, and therefore exceeding component current ratings. However, testing for full-power operation at the test voltages of 230 V_{rms} and 265 V_{rms} is possible, and is undertaken

For each output power interval tested, the input power is calculated using the Simulink interface to the LAUNCHXL-F28379D, using the in-built current and voltage sensor on the primary PCB to calculate the input power. An approximate 2% variance in the input power calculation is observed during this testing when the output power is constant, indicating some measurement error in the sampling of the input voltage and current, and therefore error bars have been included in the efficiency graphs to indicate a range of realistic efficiencies.

Figure 52 shows the plotted experimental results for the efficiency across the output power range, where each series is for the input voltage indicated in the legend.

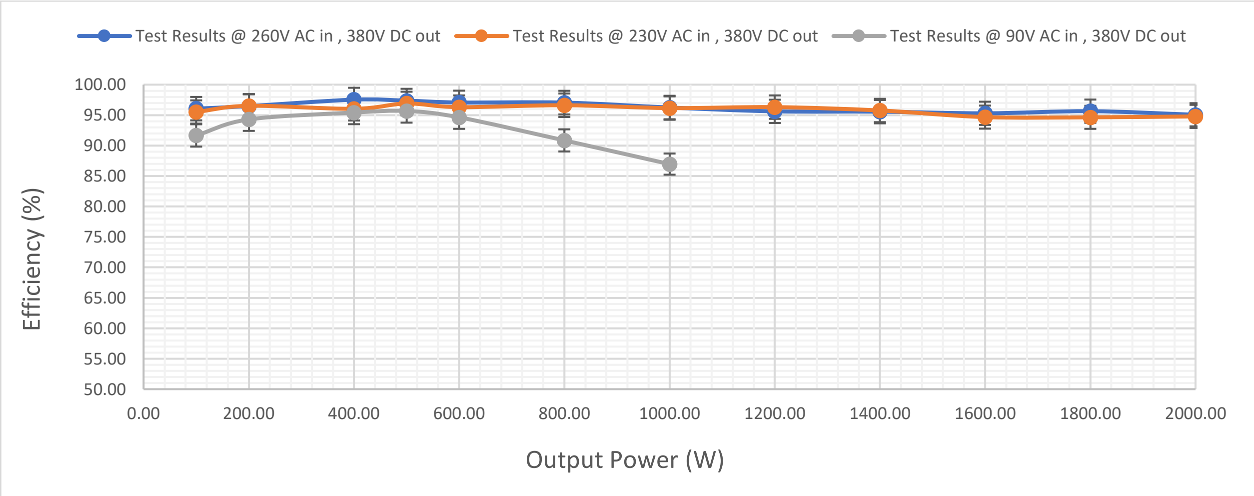

Figure 52: Efficiency across output power range

The key observation in the efficiency plot is the sharp decline in efficiency when operating with the lower end input voltage of 90 V_{rms}. This is likely caused by the high peak currents due to the lack of the active PFC control system as seen in Figure 54 and Figure 53. Higher peak currents can reduce efficiency significantly, as the conduction losses of multiple components are increased.

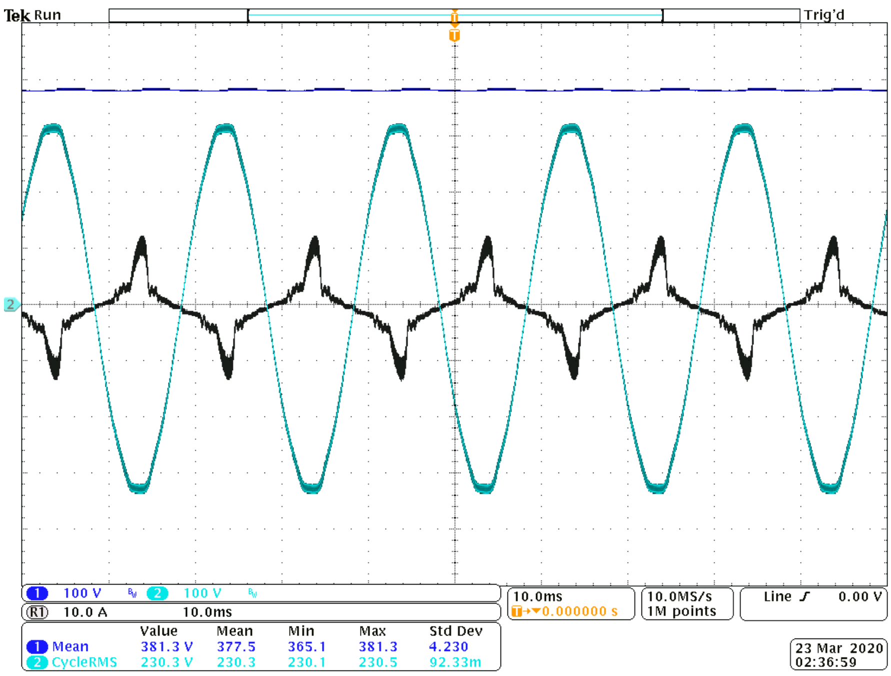

Figure 53: Input voltage and current (230 V, 1 kW)

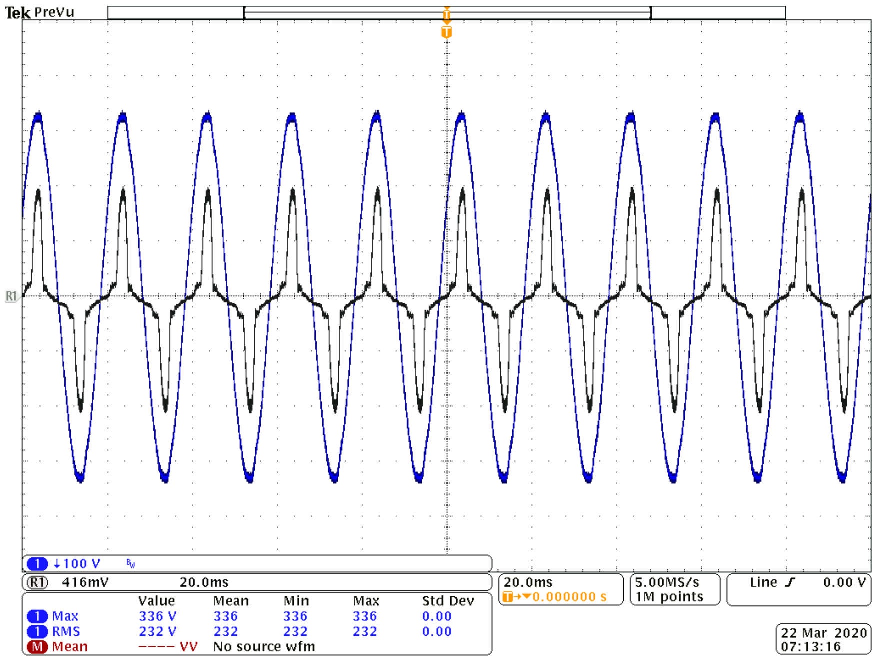

Figure 54: Input voltage and current (230 V, 2 kW)

Efficiency is also reduced when the peak currents exceed the design parameters, as the magnetic component losses increase as they near saturation. Operation at 90 V_{rms} is a potential limitation in the suitability as a shore power converter, as higher efficiencies may be harder to achieve. It is expected that this power loss will be reduced when operating with active PFC, and therefore further experimental validation is required

However, the experimental results show high efficiencies during the full range of output power at both 230 V_{rms} and 265 V_{rms} input voltages, even without the active PFC control system. This shows that the bridgeless isolated converter may be more suited to operation with a higher input voltage, as a lower voltage gain is required to produce an output voltage of 380 V_{dc}. Therefore, a potential solution for operating at higher power levels could be through the use of three-phase operation where the input voltage is the line to line voltage, thus higher voltage than a single-phase input. Further analysis would be required to investigate three-phase operation, although it has already been shown in [36].

Experimental results for the component temperatures were also recorded during the testing across the output power range so that the use of thermal models and heatsinks in the PLECS simulations could be verified. The component temperatures were observed using a FLIR One thermal camera, which also allowed the identification of other hotspots in the prototype, as seen in Figure 56 and Figure 55.

Figure 56: Thermal imaging of entire prototype

Figure 55: Thermal imaging of MOSFET package

Figure 57 and Figure 58 show the MOSFET and diode temperatures respectively across the entire output power range. The comparison is made between the experimental results and the simulation results using the same parameters of an input voltage of 230 V_{rms} and output voltage of 380 V_{dc}. The simulation parameters for both the MOSFET and the diode thermal models used an ambient temperature of 25 $°C$ and a thermal resistance of 1 $°C/W$ and 12 $°C/W$ respectively, as these are the thermal resistances of the chosen heatsinks for the prototype.

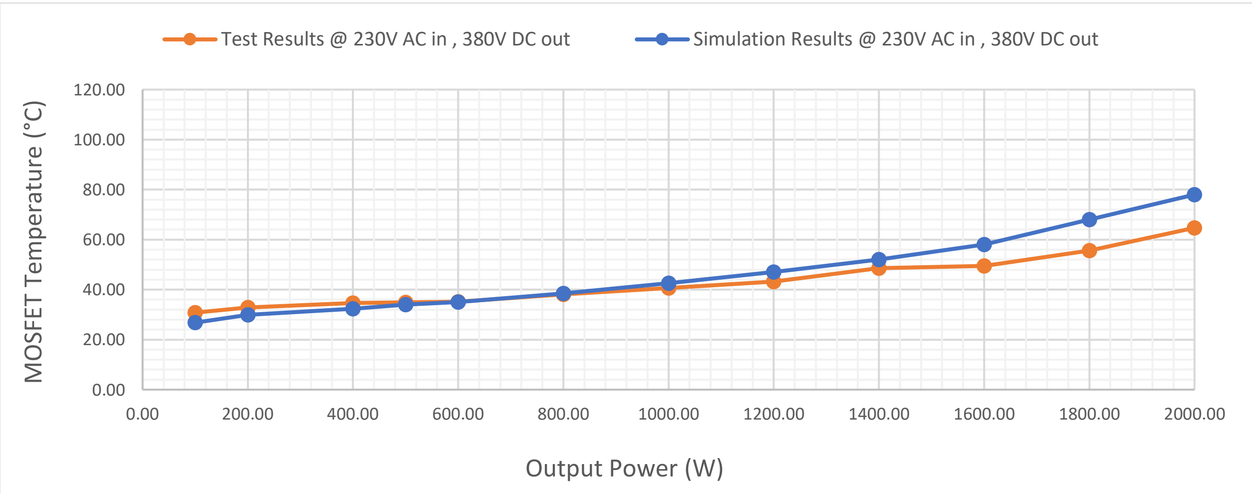

Figure 57: MOSFET temperature over the output power range

Since the experimental ambient temperature will vary from the ambient temperature in the simulation, some margin of error is expected in the results.

It is expected that the experimental results will be slightly lower than simulated, as the ambient temperature is below 25 $°C$ for most of the testing. Figure 57 and Figure 58 show that both sets of experimental data fit the simulation results very closely, with the largest error being only 5.4 % below the simulated value.

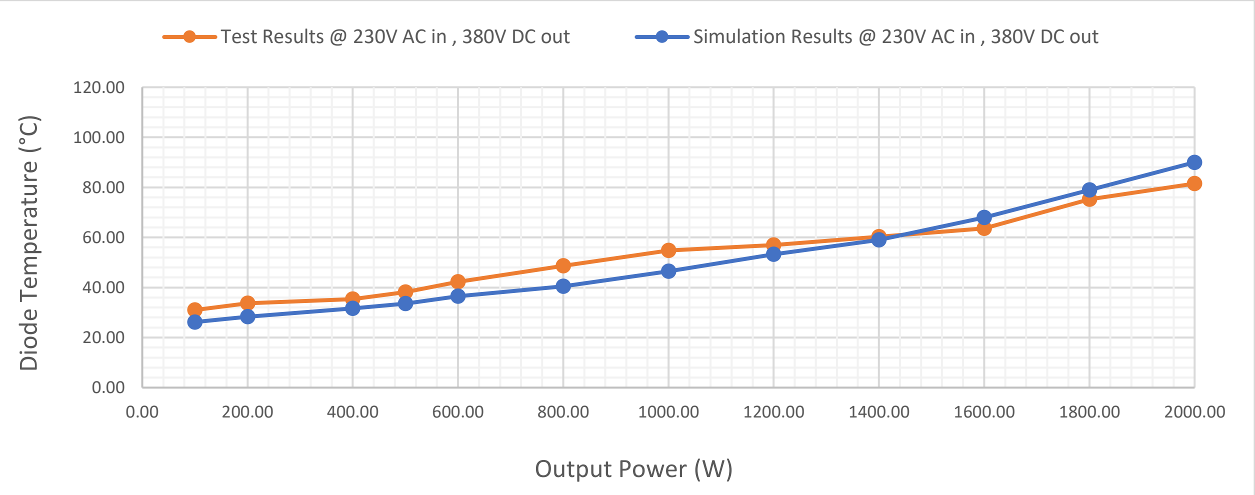

Figure 58: Output diode temperature over the output power range

While the MOSFET temperature varies from the simulated data in both directions, it is still a close agreement with the simulated values, and some of this error can be put down to measurement error in the thermal camera, or slight variances in the real MOSFET thermal model. However, it can be concluded that the thermal models are accurate for simulation and design purposes and are an invaluable resource in the prototype design.

Since operation across the range of power levels has been verified, it is desirable to investigate the accuracy of the approximations made in Section 3.2. Figure 59 shows the entire switching waveform over multiple input cycles and it can be seen that the maximum switch voltage occurs when the input current is at a peak, which is the middle of one half of the waveform, as described in Section 3.2.5 for the sizing of the resonant capacitor. The capacitor ripple voltage will vary greatly from the theory and simulation, as the duty cycle and the peak currents will be both different due to the lack of an active PFC control system, meaning that peak currents are higher than the calculated values, and therefore the duty cycle will also vary from the expected value. This means that the peak switch voltage will also vary from the expected value. However, the peak switch voltage can be calculated using the input current measured in Figure 54, and the new total resonant capacitance as calculated in Section 4.2.2.

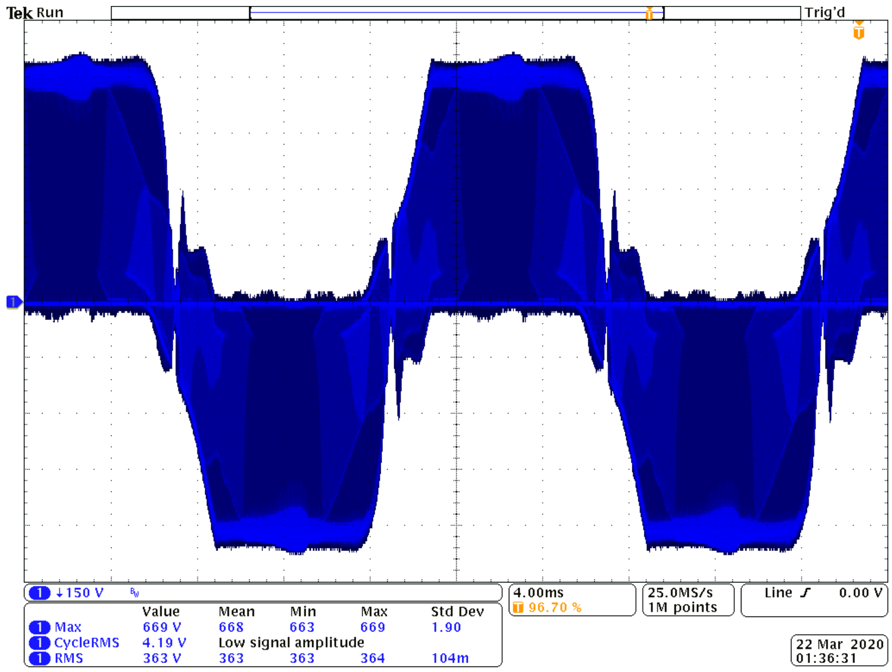

Figure 59: Switch voltage (Viewed at input frequency)

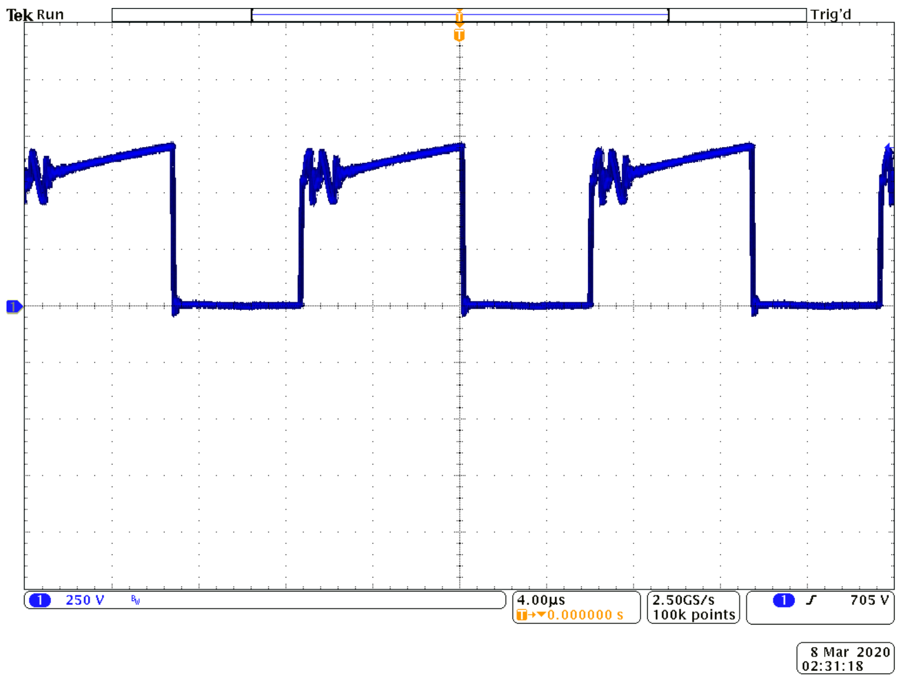

Figure 60: Switch voltage (Viewed at switching frequency)

The peak input current is measured to be 26.03 A when using a 230 V_{rms} input with 2 kW of output power. Using this measured current and the new resonant capacitance of 750 nF, the ripple voltage of the capacitor can be calculated using (3.14), allowing the peak switch voltage to be calculated using (3.13). This results in a ripple voltage ΔV_{C_r} of $247.46\ V$. Therefore, the peak switch voltage is calculated using (3.13), resulting in a peak voltage of $731\ V$.

Figure 60 shows the switch voltage at the switching frequency resolution. Measuring the peak of this waveform gives a maximum switch voltage of 730 V which further confirms the accuracy of the linear approximation made in Section 3.2.4. Although the approach in Section 3.2.4 requires knowledge of the peak input current, most designs of the bridgeless isolated converter will implement active PFC and, therefore, a sinusoidal approximation of the input current is reasonable, which eases determination of the peak current.

Figure 59 and Figure 60 also show that the average switch voltage during t_{off} is approximately 610 V, which shows close agreement to the average switch voltage of 608 V calculated in Section 3.2.4. A small error may be attributed to transformer regulation, making the reflected transformer voltage differ slightly with simulated and calculated values.

To confirm the transformer winding ratio, the waveforms of the primary and secondary transformer windings can be used. Figure 61 and Figure 62 show the primary and secondary winding voltages respectively. It is apparent no DC offset exists, and that the transformer is volt-second balanced at the switching frequency.

The winding ratio of the transformer can be confirmed using the cycle RMS values measured with the oscilloscope. The measured primary voltage is $293\ V_{rms}$, and the measured secondary voltage is $366\ V_{rms}$. The winding ratio n is calculated to be 1.2492. This shows that the winding ratio is in agreement with the designed values. Differences are attributed to transformer regulation.

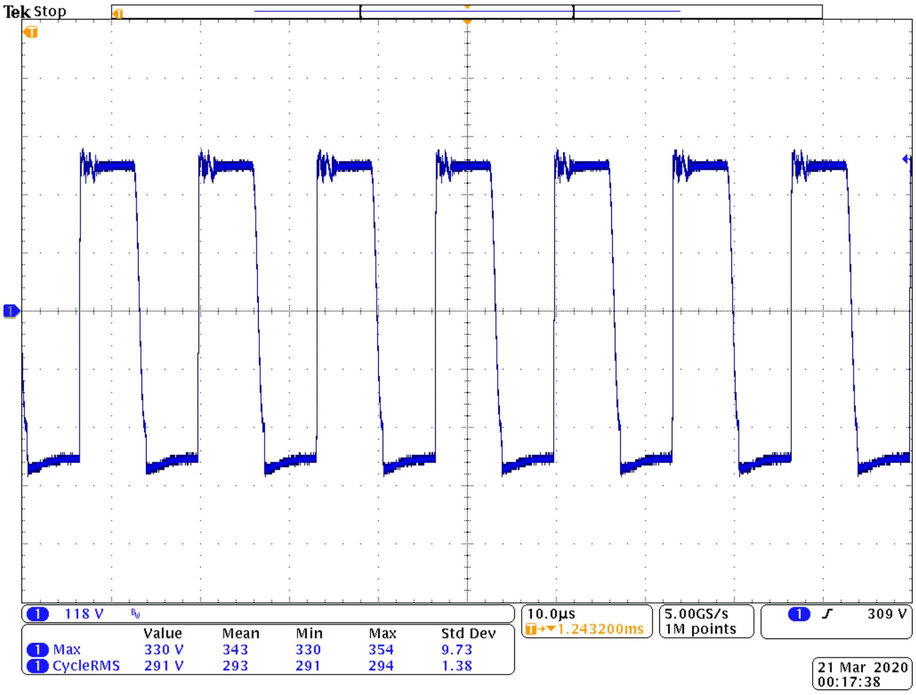

Figure 61: Transformer primary voltage

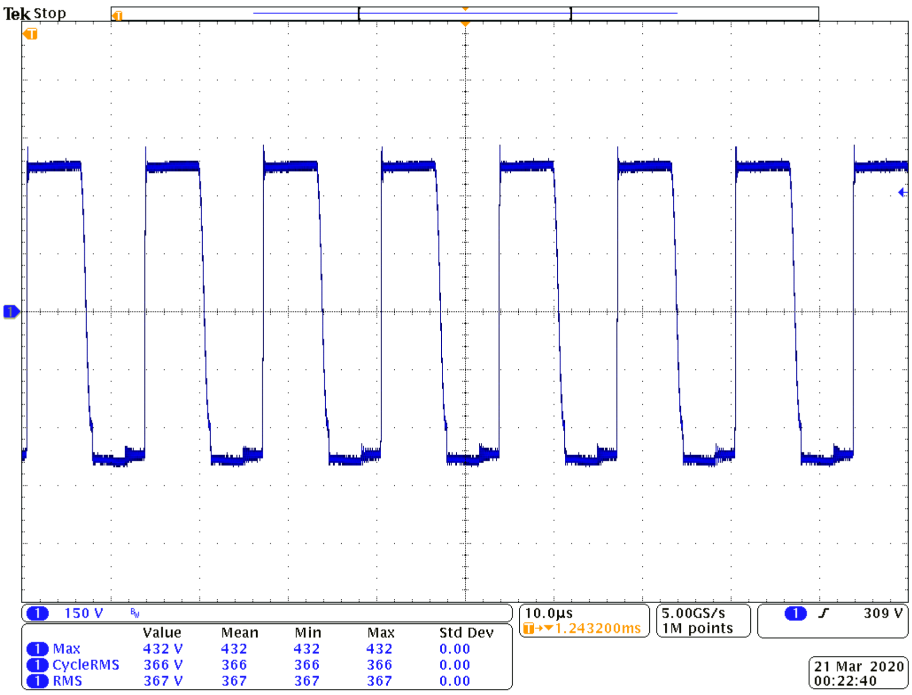

Figure 62: Transformer secondary voltage

5.4 Conclusion

Chapter 5 presented the successful design and implementation of a prototype bridgeless isolated converter first proposed in [8]. The bridgeless isolated converter is designed to operate with a wide input voltage of 90 V_{rms} to 300 V_{rms}, an output power of 2 kW at an output voltage of 380 V_{dc}. It was verified over an input range of 90 V_{rms} to 265 V_{rms} due to limitations in the available power supplies. The output voltage is shown to be regulated at 380 V_{dc} across the tested range of input voltages, and 2 kW output power is achieved at 230 V_{rms} and 265 V_{rms}. Limitations in the wide input voltage pose a significant concern in the suitability of the use of the bridgeless isolated converter in a shore power converter, although this may be alleviated through the implementation of active PFC.

Although the operation of the bridgeless isolated converter has been successfully confirmed, active PFC was not implemented due to time constraints. However, it was shown that the bridgeless isolated converter can perform with an active PFC control system in Section 4.4, and complies with IEC 61000-3-12 harmonic standard limits, without the need for an input filter. Therefore, by implementing active PFC, it is expected that the bridgeless isolated converter will meet the active PFC requirements of a shore power converter. It is also shown in this chapter that the bridgeless isolated converter can achieve galvanic isolation through a high-frequency transformer. This verifies that the bridgeless isolated converter can realise the proposed weight reductions if used to implement a shore power converter.

Chapter 6

Conclusion

6.1 Introduction

Chapter 1 has introduced the need for a shore power converter when a marine vessel is connecting to a shore supply, due to the requirements of galvanic isolation, and varying voltage supplies when a vessel travels internationally. This chapter also introduced the key requirements that a shore power converter will need to fulfil and the areas of improvement that can be developed on. A proposed solution to this area of improvement is the use of a high-frequency transformer to provide galvanic isolation, as the size and weight of the shore power converter can be reduced. The size and weight of some existing commercial solutions are analysed.

Chapter 2 investigated existing AC/AC topologies and showed the need for the use of a DC-link converter when frequency conversion is required. Research into DC-link converters showed that the key area for improvement is in the AC/DC conversion stage, as a multi-stage approach is commonly used to incorporate high-frequency isolation. A suggested solution to this area of improvement is the use of a single-stage converter that can incorporate the key features of active PFC, voltage conversion, and high-frequency isolation into a single stage. One converter topology found in the literature review is the bridgeless isolated converter, which is unique in its 'true bridgeless' [36] approach to active PFC and galvanic isolation, using a single switch with no input rectifier. Research gaps were identified in the bridgeless isolated converter, especially concerning the design of the resonant circuit, as many considerations need to be made to optimally design this section of the converter, yet no design procedure is seen in the existing literature.

Chapter 3 introduces the design of the bridgeless isolated converter and derives the voltage conversion ratio by applying the volt-second rule to the input inductor L_i. The input inductor L_i is then designed for a specified ripple current. Expressions derived during these processes are then used to build upon a design procedure for the resonant circuit, which satisfies the research questions. The remaining components and operation of the converter are then designed.

Chapter 4 verifies the theoretical design through simulation in PLECS, where the design procedure is confirmed with a small margin of error in the approximations. The active PFC control system for the bridgeless isolated converter is then designed and simulated to show the improvements in harmonic content when operating with active PFC and prove the bridgeless isolated converter can perform both output voltage regulation and active PFC with a single switch. Comparison is then made to the IEC 61000-3-12 standard to prove that the converter has the capability to meet the PFC requirements of a shore power converter.

Chapter 5 details the experimental prototype and test results of the bridgeless isolated converter. This is used to confirm aspects of the simulation such as the PLECS thermal model results and verify the resonant design procedure is accurate even when the input current is not sinusoidal. Although active PFC is not implemented, the converter is shown to operate across a wide input voltage range while having a constant regulated output voltage, and operation up to 2 kW is achieved with high efficiencies > 90 % with input voltages greater than $230\ V_{rms}$. The weight of the converter is then analysed and compared to the existing shore power converters introduced in Chapter 1, showing a significant weight reduction and verifying the suggested solution of reducing weight using a high-frequency transformer.

6.2 Research Questions

In this section, the research questions are given and addressed based on the research presented in this thesis. A critical evaluation of the research questions is made, and future work is introduced.

- Can a detailed design procedure for the resonant components improve the operation of the bridgeless isolated converter?

The design procedure is shown in Chapter 3 as a method to optimise the choice in resonant components. The design procedure follows four key steps to optimally design the resonant circuit. By following these steps, the resonant circuit can be optimized for the required operation of the converter. This allows the design of the resonant frequency to be made considering the expected gain required for the application, which then allows the resonant capacitance to be designed for a specific switch voltage to avoid having to use higher-rated switches than required, which often have much worse characteristics than lower-rated switches of the same series. The leakage inductance is then set based on a minimum achievable leakage inductance of the transformer. The full range of resonant components is then derived from these minimum values and the resonant frequency. This is an improvement on the typical design approach of designing the circuit components first and choosing semiconductors that fit the outcome of the component design, as the new design procedure considers both parameters simultaneously, and therefore avoids the use of over-rated components which is typical in poorly designed circuits.

This design procedure is confirmed through simulation shown in Chapter 4, and it is clearly shown that using the components within the optimal range results in lower switch stresses and allows the use of lower-rated switches, thereby improving the efficiency of the converter. This is a significant contribution as the components for the converter can be optimized, and semiconductor selection considered at the start of the design process, rather than as an afterthought.

- Is the bridgeless isolated converter topology operating with active power factor correction suited to the power levels required for a shore power converter?

It is shown in Chapter 5 that the bridgeless isolated converter is successfully prototyped. Operation at 2 kW is shown, although at the lower input voltage of 90 V_{rms} the full output power of 2 kW is not able to be achieved. This is due to the high peak currents drawn by the converter when an active PFC control system is not used. While this is one limitation of the bridgeless isolated converter, it is shown in Chapter 4 that realistic simulations of the bridgeless isolated converter confirm its operation with active PFC across the entire input voltage range and that the harmonic content is reduced to acceptable levels, even without the use of an input filter. Chapter 5 also shows the successful implementation of a high-frequency transformer to provide galvanic isolation, and therefore it has been shown through various parts of this thesis that the bridgeless isolated converter can meet the requirements that were outlined in Chapter 1. The design of the experimental prototype also showed a significant weight reduction compared to existing shore power converters which implement a mains frequency transformer.

However despite these requirements being met, operation with active PFC would need to be proven experimentally, and since the bridgeless isolated converter only forms half of the entire shore power converter, an inverter stage would also need to be modelled to form the entire converter before a clear conclusion can be made on the suitability. While this shows that significant future work is required, it has been shown in this thesis that the bridgeless isolated converter is capable of realising the proposed advantages in weight reduction, using a bridgeless single-stage, single-switch design.

6.3 Future Work

Future work is required in order to provide further insight into the suitability of the bridgeless isolated converter as the input stage for a shore power converter. It is required that active PFC is implemented in the bridgeless isolated converter prototype to confirm the simulated active PFC operation shown in Chapter 4, and to further examine EMC suitability. This is significant as the shore power converter would be required to operate at high power levels. Therefore, harmonic content can potentially become a significant issue if active PFC operation is not confirmed. The implementation of active PFC would also need to result in an improved voltage control system, to optimize the regulation of the output voltage.

Other future work regarding the high-power operation of the bridgeless isolated converter would involve an investigation into the three-phase operation of the converter, as this can reduce the size of the DC bus capacitors and increase the operating power of the converter. A shore power converter will also require an input filter to limit EMI further, and an output inverter is required to be designed in order to create the required AC output voltages suitable for the vessel's requirements.

While there is some future work required, significant discoveries have been made, and the knowledge base of the bridgeless isolated converter has been contributed to significantly through the introduction and verification of a design procedure for the resonant circuit.

Appendix

Minimum R_{sce}	Admissible individual harmonic current I_h/I_{ref} [a] %						Admissible harmonic parameters %	
	I_3	I_5	I_7	I_9	I_{11}	I_{13}	THC/I_{ref}	$PWHC/I_{ref}$
33	21,6	10,7	7,2	3,8	3,1	2	23	23
66	24	13	8	5	4	3	26	26
120	27	15	10	6	5	4	30	30
250	35	20	13	9	8	6	40	40
≥350	41	24	15	12	10	8	47	47

The relative values of even harmonics up to order 12 shall not exceed $16/h$ %. Even harmonics above order 12 are taken into account in *THC* and *PWHC* in the same way as odd order harmonics.

Linear interpolation between successive R_{sce} values is permitted.

[a] I_{ref} = reference current; I_h = harmonic current component.

Appendix 1: IEC 61000-3-12 Table 2 - limits for harmonic content

References

[1] *BS IEC/IEEE 80005-1:2019 Utility connections in port High voltage shore connection (HVSC) systems. General requirements*. BSI Standards Limited, 2019.

[2] *BS IEC/IEEE 80005-3. Utility connections in port. Part 3. Low Voltage Shore Connection (LVSC) Systems. General requirements*. BSI Standards Limited, 2016.

[3] “About - ASEA Power Systems,” *ASEA Power Systems*. [Online]. Available: https://aseapower.com/about/#story. [Accessed: 01-Feb-2020].

[4] “AC Series - ASEA Power Systems,” *ASEA Power Systems*. [Online]. Available: https://aseapower.com/product/ac-series-converter/. [Accessed: 01-Feb-2020].

[5] “Q Series - ASEA Power Systems,” *ASEA Power Systems*. [Online]. Available: https://aseapower.com/product/q-series-converter/. [Accessed: 01-Feb-2020].

[6] “ShorPOWER ULTRA LP - Shore Power Frequency Converter for Yachts | Atlas Marine Systems,” *Atlas Marine Systems*. [Online]. Available: https://www.atlasmarinesystems.com/products/shorpower-ultra-lp/. [Accessed: 01-Feb-2020].

[7] “Magnus Marine - Yacht Shore Power Converter| SP100 | Magnus Marine,” *Magnus Marine*. [Online]. Available: http://www.magnusmarine.com/products/yacht-shore-power-converters/sp100. [Accessed: 01-Feb-2020].

[8] S. Cuk, “Single–Stage Bridgeless Isolated PFC Converter Achieves 98% Efficiency,” *Power Electron. Technol.*, no. October, pp. 22–31, 2010.

[9] Y. Jang and M. M. Jovanović, “Fully soft-switched three-stage ac-dc converter,” *IEEE Trans. Power Electron.*, vol. 23, no. 6, pp. 2884–2892, 2008.

[10] G. Parise, L. Parise, and M. Mitolo, “Grounding system in Marinas: The microsystem approach,” *IEEE Trans. Ind. Appl.*, vol. 47, no. 5, pp. 2204–2209, 2011.

[11] P. R. Mohanty, A. K. Panda, and D. Das, “An active PFC boost converter topology for power factor correction,” *12th IEEE Int. Conf. Electron. Energy, Environ. Commun. Comput. Control (E3-C3), INDICON 2015*, pp. 1–5, 2016.

[12] K. Liu and L. Li, “Analysis of favored design frequency of high-frequency transformer with different power capacities,” in *POWERCON 2014 - 2014 International Conference on*

Power System Technology: Towards Green, Efficient and Smart Power System, Proceedings, 2014, pp. 2272–2278.

[13] A. A. Khan, H. Cha, and H. F. Ahmed, “Double step-down AC-AC converters with high frequency isolation,” *2016 IEEE 8th Int. Power Electron. Motion Control Conf. IPEMC-ECCE Asia 2016*, pp. 1200–1205, 2016.

[14] M. Jagau and M. Patt, “Reactive power operation of a single phase AC-AC DAB converter,” *PCIM Eur. 2017 - Int. Exhib. Conf. Power Electron. Intell. Motion, Renew. Energy Energy Manag.*, no. May, pp. 16–18, 2017.

[15] U. Nasir, A. Costabeber, M. Rivera, P. Wheeler, and J. Clare, “A Leakage-Inductance-Tolerant Commutation Strategy for Isolated AC/AC Converters,” *IEEE J. Emerg. Sel. Top. Power Electron.*, vol. 7, no. 1, pp. 467–479, 2019.

[16] P. W. Wheeler, J. Rodríguez, J. C. Clare, L. Empringham, and A. Weinstein, “Matrix converters: A technology review,” *IEEE Trans. Ind. Electron.*, vol. 49, no. 2, pp. 276–288, 2002.

[17] E. D. Binti Rosli, M. N. Bin Hidayat, and R. Bin Baharom, “Direct single phase AC-AC dynamic voltage restorer,” *Proc. Int. Conf. Power Electron. Drive Syst.*, pp. 1257–1262, 2013.

[18] G. Aarthi and T. Porselvi, “Modeling and simulation of single phase matrix converter using PWM,” *2012 Int. Conf. Comput. Electron. Electr. Technol. ICCEET 2012*, pp. 168–173, 2012.

[19] H. Keyhani and H. A. Toliyat, “Isolated ZVS high-frequency-link AC-AC converter with a reduced switch count,” *IEEE Trans. Power Electron.*, vol. 29, no. 8, pp. 4156–4166, 2014.

[20] O. C. Silva Filho, B. R. De Almeida, D. S. Oliveira, and T. R. F. Neto, “Loss analysis of a high frequency isolated AC-AC converter applied as voltage regulator,” *14th Brazilian Power Electron. Conf. COBEP 2017*, vol. 2018-Janua, no. 85, pp. 1–6, 2017.

[21] F. Liu, X. Ruan, X. Huang, and Y. Qiu, “Second Harmonic Current Reduction for Cascaded Inverter with Pre-regulator + LLC Converter as Front-End DC − DC Converter,” *2019 IEEE Energy Convers. Congr. Expo.*, pp. 686–690, 2019.

[22] A. S. S. F. Converter, H. Chiu, Y. Lo, H. Lee, S. Cheng, and S. Mou, “A Single-Stage Soft-Switching Flyback Converter for Power-Factor-Correction Applications,” vol. 57, no. 6, pp. 2187–2190, 2010.

[23] X. Chen, T. Jiang, X. Huang, and J. Zhang, "A high efficiency bridgeless flyback PFC converter for adapter application," *Conf. Proc. - IEEE Appl. Power Electron. Conf. Expo. - APEC*, pp. 1013–1017, 2013.

[24] J. Baek, J. Shin, P. Jang, and B. Cho, "A critical conduction mode bridgeless flyback converter," in *8th International Conference on Power Electronics - ECCE Asia: "Green World with Power Electronics", ICPE 2011-ECCE Asia*, 2011, pp. 487–492.

[25] R. Kushwaha and B. Singh, "An improved power quality based PFC converter for EV battery charger," in *IEEE International Conference on Power Electronics, Drives and Energy Systems, PEDES 2016*, 2017, vol. 2016-January, pp. 1–6.

[26] T.-F. Wu and J.-C. Hung, "Development of ZVS single-stage isolated converters with a PFC feature based on asymmetrical half-bridge topology," 2003, pp. 1363–1368.

[27] J. Wang, L. Hou, and K. Wu, "Investigation of an isolated PFC converter with bridgeless and single-stage," in *2017 IEEE 3rd International Future Energy Electronics Conference and ECCE Asia, IFEEC - ECCE Asia 2017*, 2017, pp. 1266–1269.

[28] T. Tanitteerapan and S. Mori, "Simplified input current waveshaping technique by using inductor voltage sensing for power factor correction isolated Sepic rectifier," 2003, pp. IV-345-IV–348.

[29] S. Y. Chen, Z. R. Li, and C. L. Chen, "Analysis and design of single-stage AC/DC LLC resonant converter," *IEEE Trans. Ind. Electron.*, vol. 59, no. 3, pp. 1538–1544, 2012.

[30] C. Lai, S. Member, and R. Lee, "A Single-Stage AC / DC LLC Resonant Converter," pp. 1386–1390, 2006.

[31] S. Nigsch, S. Cuk, and K. Schenk, "Analysis, modeling and design of a True Bridgeless Single Stage PFC with galvanic isolation," in *Conference Proceedings - IEEE Applied Power Electronics Conference and Exposition - APEC*, 2015, vol. 2015-May, no. May, pp. 469–476.

[32] D. Bortis, L. Fassler, and J. W. Kolar, "Comprehensive analysis and comparative evaluation of the isolated true bridgeless Cuk single-phase PFC rectifier system," in *2013 IEEE 14th Workshop on Control and Modeling for Power Electronics, COMPEL 2013*, 2013.

[33] R. L. Steigerwald, "A comparison of half-bridge resonant converter topologies," *APEC 1987 - 2nd Annu. IEEE Appl. Power Electron. Conf. Expo. Conf. Proc.*, vol. 3, no. 2, pp. 135–144, 2015.

[34] A. Fehér and Z. Puklus, "Definitions and measurement of power factor," *8th Int. Symp. Hungarian Res. Comput. Intell. Informatics, CINTI 2007*, pp. 623–632, 2007.

[35] N. O. Copying, W. Bsi, P. Except, A. S. Permitted, and B. Y. Copyright, "BSI Standards Publication Electromagnetic compatibility (EMC)," no. April 2013, 2010.

[36] S. Cuk, "Part 2 bridgeless PFC converter achieves 98% efficiency, 0.999 power factor," *Power Electron. Technol.*, vol. 36, no. 8, pp. 34–40, 2010.

[37] H. F. Ahmed, H. Cha, A. A. Khan, and H. G. Kim, "A single-phase high-frequency transformer isolated buck converter with both in-phase and out-of-phase operations," *2016 IEEE 8th Int. Power Electron. Motion Control Conf. IPEMC-ECCE Asia 2016*, pp. 2204–2208, 2016.

[38] H. F. Ahmed, H. Cha, A. A. Khan, and H. G. Kim, "A Highly Reliable Single-Phase High-Frequency Isolated Double Step-Down AC-AC Converter with Both Noninverting and Inverting Operations," *IEEE Trans. Ind. Appl.*, vol. 52, no. 6, pp. 4878–4887, 2016.

[39] Z. Zhang, A. Mallik, and A. Khaligh, "A high step-down isolated three-phase AC-DC converter," *IEEE J. Emerg. Sel. Top. Power Electron.*, vol. 6, no. 1, pp. 129–139, Mar. 2018.

[40] O. Cipriano Da Silva Filho, B. R. De Almeida, D. De Souza Oliveira Junior, and T. R. Fernandes Neto, "High-Frequency Isolated AC-DC-AC Interleaved Converter for Power Quality Applications," *IEEE Trans. Ind. Appl.*, vol. 54, no. 5, pp. 4594–4602, 2018.

[41] H. L. Cheng, C. A. Cheng, and C. S. Chang, "A novel single-stage HPF AC/DC converter with integrated buck-boost and flyback converters," in *ISNE 2013 - IEEE International Symposium on Next-Generation Electronics 2013*, 2013, pp. 146–149.

[42] R. Beiranvand, S. Salehirad, and S. Esmailirad, "Analysis of a bridgeless single stage pfc based on LLC resonant converter for regulating output voltage," *2019 IEEE 31st Int. Conf. Microelectron. MIEL 2019 - Proc.*, pp. 353–356, 2019.

[43] J. Gottle and T. Durbaum, "A resonant single-stage PFC AC-DC converter," in *Proceedings - 2015 9th International Conference on Compatibility and Power Electronics, CPE 2015*, 2015, pp. 352–358.

[44] M. Scherbaum, M. Reddig, R. Kennel, and M. Schlenk, "An Isolated, bridgeless, quasi-resonant ZVS-switching, buck-boost single-stage AC-DC converter with power factor correction (PFC)," in *Conference Proceedings - IEEE Applied Power Electronics Conference and Exposition - APEC*, 2017, pp. 74–81.

[45] C. D. Davidson, “Single stage true bridgeless AC/DC power factor corrected converter,” in *INTELEC, International Telecommunications Energy Conference (Proceedings)*, 2016, vol. 2016-September.